Check for updates

Author Manuscript

Title: Systematic influence of electronic modification of ligand on the catalytic rate of water oxidation by a single-site Ru-based catalyst

Authors: Jully Patel, Ph.D; Gabriel Bury; Alireza K. Ravari, Ph.D; Roman Ezhov, Ph.D; Yulia Pushkar, Ph.D

This is the author manuscript accepted for publication. It has not been through the copyediting, typesetting, pagination and proofreading process, which may lead to differences between this version and the Version of Record.

To be cited as: 10.1002/cssc.202101657

Link to VoR: https://doi.org/10.1002/cssc.202101657

Systematic influence of electronic modification of ligand on the catalytic rate of water oxidation by a single-site Ru-based catalyst

Dr. Jully Patel, Gabriel Bury, Dr. Alireza K. Ravari, Dr. Roman Ezhov, and Prof. Yulia Pushkar*[a]

[a]Department of Physics and Astronomy, Purdue University, West Lafayette, Indiana 47907, United States

*corresponding author ypushkar@purdue.edu

This article is protected by copyright. All rights reserved

Author Manuscript

1864564x, 2022, 4, Downloaded from https://chemistry-europe.onlinelibrary.wiley.com/doi/10.1002/cssc.202101657 by Office Of Scientific And Technical Information, Wiley Online Library on [28/09/2023]. See the Terms and Conditions (https://onlinelibrary.wiley.com/terms-and-conditions) on Wiley Online Library for rules of use; OA articles are governed by the applicable Creative Commons License

Abstract

Catalytic water oxidation is an important process for the development of future clean energy solutions and energy storage. Despite the significant number of reports on active catalysts, systematic control of the catalytic activity remains elusive. Here, we continue to explore descriptors which can be correlated with catalytic activity. [Ru(tpy)(pic)$_2$(H$_2$O)](NO$_3$)$_2$, **1**, and [Ru(EtO-tpy)(pic)$_2$(H$_2$O)](NO$_3$)$_2$, **2**, (where tpy = 2,2′:6′,2″-terpyridine, EtO-tpy = 4′-(ethoxy)-2,2′:6′,2″-terpyridine, pic = 4-picoline) have been synthesized and characterized by NMR, UV-vis, electrochemical analysis, EPR, resonance Raman, and X-ray absorption spectroscopy. Addition of the ethoxy group increases catalytic activity in chemically driven and photocatalytic water oxidation. Thus, the effect of the electron-donating group known for the [Ru(tpy)(bpy)(H$_2$O)]$^{2+}$ family is transferable to architectures with a tpy ligand trans to the Ru-oxo unit. Under catalytic conditions, **2** displays new spectroscopic signals tentatively assigned to a peroxo intermediate. Reaction pathways were analyzed using DFT. Currently, **2** is one of the most active catalysts functioning via a water nucleophilic attack mechanism.

TOC:

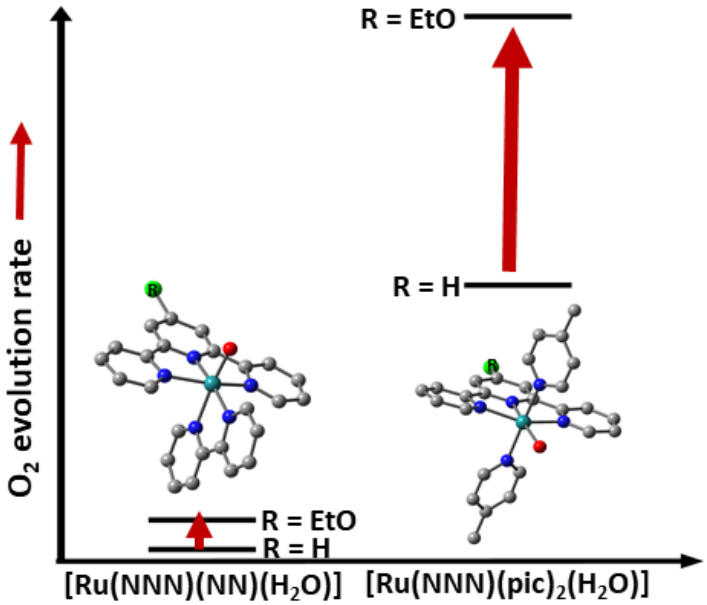

Increasing the catalytic rate of water oxidation by Ru molecular catalysts: Catalytic water oxidation is an important process for the development of future clean energy solutions. While Ru catalysts are the most studied in the field, we still did not reach the limit of their activity. Here, electronic modification of the ligand environment – addition of an electron donating group – increases catalytic performance; our comprehensive study of the mechanism yields valuable insights for future rational catalyst design.

KEYWORDS: Homogeneous catalysis, Water oxidation, Ruthenium, reactive intermediates, EPR, resonance Raman.

This article is protected by copyright. All rights reserved

Author Manuscript

1864564x, 2022, 4, Downloaded from https://chemistry-europe.onlinelibrary.wiley.com/doi/10.1002/cssc.202101657 by Office Of Scientific And Technical Information, Wiley Online Library on [28/09/2023]. See the Terms and Conditions (https://onlinelibrary.wiley.com/terms-and-conditions) on Wiley Online Library for rules of use; OA articles are governed by the applicable Creative Commons License

Introduction:

Increasing population and economic growth contributes to the tremendous energy demand, estimated to double by the year 2040.[1] Given the limited supply of fossil fuels, this demands change in the world energy consumption. Therefore, there is an urgent need for clean and renewable energy sources as alternatives to fossil fuel.[1, 2] Water splitting to generate chemical energy in artificial photosynthesis is the most favourable pathway for the development of clean and renewable energy.[3-5] In nature, the chemical conversion of solar energy starts with the water oxidation reaction (WOR), generating O_2, catalysed by the μ-oxo-bridged tetramanganese cluster present in the oxygen evolving complex (OEC) of Photosystem II.[5-9] This functional aspect of the OEC may provide a possible path for the design of efficient catalysts for artificial photosynthesis. In the last decade, various water oxidation catalysts (WOCs) have been developed based on ruthenium,[10-14] manganese,[15-19] iron,[20-23] and iridium.[24-27] Integrated systems with chromophore-catalyst assemblies[28-31] and catalysts incorporated into metal-organic frameworks (MOF)s were also reported[32-36] .

A desired water oxidation catalyst should have a simple structure, able to be modified to control activity. The catalyst should be stable under catalytic conditions. Most importantly, it should function at low overpotential, making the process energetically efficient. Water oxidation typically involves multiple proton-coupled electron transfer (PCET) steps producing intermediates with various valence states. The O–O bond formation is triggered by high valent metal-oxo species, often postulated as the crucial intermediates.[21, 37, 38] Over decades, both dinuclear and mononuclear Ru(II) polypyridine catalysts have attracted great attention from researchers. During this time, many different series of Ru-based WOCs were synthesized and analysed.[39-43] Ru complexes are highly active, relatively stable in harsh WOR conditions, easy to synthesize, and amenable to structural modifications. The higher oxidation states of Ru can be observed under catalytic conditions, facilitating mechanistic insights.[37, 44]

In 1982, Meyer and his group reported the first molecular catalyst for water oxidation: a dinuclear ruthenium complex *cis,cis*-$[(bpy)_2(H_2O)Ru(\mu\text{-}O)Ru(H_2O)(bpy)_2]^{4+}$ (where bpy = 2,2'-bipyridine).[45, 46] Various mechanistic paths were previously considered for this complex; the latest experimental results, however, indicate that the water oxidation takes place by the nucleophilic attack of H_2O molecule on the Ru^V=O species.[47]

This article is protected by copyright. All rights reserved

1864564x, 2022, 4, Downloaded from https://chemistry-europe.onlinelibrary.wiley.com/doi/10.1002/cssc.202101657 by Office Of Scientific And Technical Information, Wiley Online Library on [28/09/2023]. See the Terms and Conditions (https://onlinelibrary.wiley.com/terms-and-conditions) on Wiley Online Library for rules of use; OA articles are governed by the applicable Creative Commons License

Author Manuscript

Different series of WOCs of [Ru(NNN)(NN)X] and [Ru(NNN)(pic)$_2$X] scaffolds (where NNN = tridentate polypyridyl ligand; NN = bidentate polypyridyl ligand; X = H_2O or halide: pic = 4-picoline) have been reported.[48] The photocatalytic activity of many of these complexes were studied using the photosensitizer $[Ru(bpy)_3]^{2+}$ and $Na_2S_2O_8$ sacrificial electron acceptor.[49-52] It was shown that by modifying both NNN and NN ligand backbones with various electron-withdrawing and electron-donating groups (*i.e.* -OMe, -NH_2, -NO_2, and -COOH), catalytic activity in water oxidation can be controlled.[53-55] The presence of an electron-withdrawing group in either the bipyridine frame or in terpyridine frame in [Ru(NNN)(NN)X] complexes decreased the catalytic rate, whereas a similar modification with an electron-donating group increases the activity, Table 1.

For instance, Yagi *et al.* reported a series of mononuclear ruthenium mono-aquo complexes of $[Ru(R\text{-}tpy)(bpy)(H_2O)]^{2+}$ (R-tpy = 2,2:6,2-terpyridine derivatives) and demonstrated that their catalytic activity for water oxidation changes with different chemical modifications of the tpy ligand.[56] The increased rate of O_2 evolution in the presence of the -EtO group was explained by the decreased redox potential of the complex, easing access to a Ru^V=O state. However, the Ru^V=O state in this catalyst remains undetected.[57] The reported pKa value (10.4) of an Ru^{II}-aquo ligand of $[Ru(tpy)(bpy)(H_2O)]^{2+}$ is significantly higher than in the complexes having $[Ru(R\text{-}tpy)(bpy)(H_2O)]^{2+}$ scaffolds (≤9), and the increased basicity of the ruthenyl oxo as an active form is expected to parallel that of the aquo oxo on Ru^{II}. Hence, the increase in the basicity of an aquo-oxo species was proposed to contribute to high catalytic activity.[56]

The main drawback of the ruthenium complexes containing neutral ligands is the difficulty of achieving the high oxidation states such as Ru^V.[57, 58] To overcome this issue, Sun and co-workers introduced negatively charged ligands with carboxylate groups.[59] The $[Ru(bda)(pic)_2]$ (H_2bda = 2,2′-bipyridine- 6,6′-dicarboxylic acid) complex is very active towards water oxidation.[59-65] Due to the intermolecular interactions and radical coupling involved in the rate-determining step, O_2 evolution has second-order kinetics with respect to this catalyst.[66] Concepción and group reported a Ru complex containing an analogous $bpaH_4$ (2,2'-bipyridine-6,6'-diphosphonic acid) ligand, wherein the ligand provides the electron donation and charge reimbursement through deprotonation from its phosphonic acid group, increasing catalyst solubility.[67] In 2015, Llobet and group reported a new family of complexes with a $[Ru(tda)(py)_2(H_2O)]$ scaffold by introducing the carboxylate group to the tpy ligand. They found that these compounds are not active in acidic conditions, but they show promising catalytic activity in basic conditions.[68] Strong σ-donation of the carboxylate group in

This article is protected by copyright. All rights reserved

Author Manuscript

1864564x, 2022, 4, Downloaded from https://chemistry-europe.onlinelibrary.wiley.com/doi/10.1002/cssc.202101657 by Office Of Scientific And Technical Information, Wiley Online Library on [28/09/2023]. See the Terms and Conditions (https://onlinelibrary.wiley.com/terms-and-conditions) on Wiley Online Library for rules of use; OA articles are governed by the applicable Creative Commons License

[Ru(tda)(py)$_2$(H$_2$O)] complexes is expected to stabilize the 7-coordinated [Ru^{IV}=O] active intermediate.

Activity of the WOC with a [Ru(NNN)(NN)(H$_2$O)] scaffold was enhanced by introducing the electron-donating group to the equatorial (NNN) ligand backbones. Previously, our group studied WOR promoted by [Ru(EtO-tpy)(bpy)(H$_2$O)]$^{2+}$ and [Ru(tpy)(bpy)(H$_2$O)]$^{2+}$ and established the reaction mechanism both computationally and experimentally.[57] Due to the presence of the EtO- group in [Ru(EtO-tpy)(bpy)(H$_2$O)]$^{2+}$ complex, the rate of O_2 evolution increased ~10 times.[56, 57] However, with the different scaffold of [Ru(bpy)$_2$(H$_2$O)$_2$]$^{2+}$, introduction of the electron-withdrawing groups was beneficial.[38] As such, we decided to investigate the [Ru(NNN)(pic)$_2$X] scaffold sensitivity to electron-donating groups. Here, we report [Ru(EtO-tpy)(pic)$_2$(H$_2$O)]$^{2+}$, **2,** (EtO-tpy = 4-ethoxy-2,2:6,2-terpyridine, pic = 4-picoline) as a new catalyst **(Figure 1)** for water oxidation with a significantly increased *k*O$_2$ and complete elimination of the lag phase in chemically driven water oxidation. Both complexes are also photoactive with $Na_2S_2O_8$ as an electron acceptor and [Ru(bpy)$_3$]Cl$_2$ as photosensitizer. We provide comparisons with the activity and electrochemical properties of the structurally similar [Ru(tpy)(pic)$_2$(H$_2$O)]$^{2+}$, **1**, and spectroscopic characterization using EPR, resonance Raman, and X-ray absorption spectroscopy. Reaction pathways were analyzed using DFT.

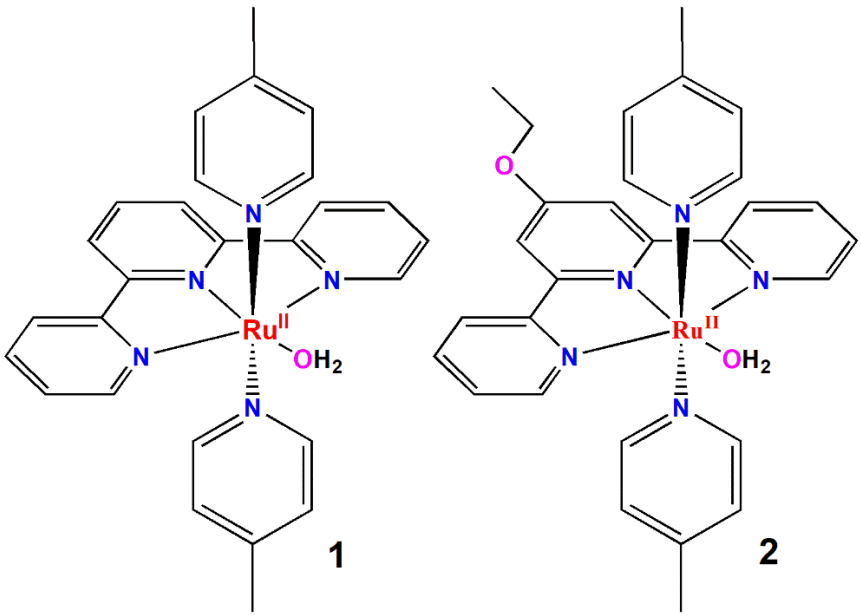

Figure 1. Structures of [Ru^{II}(tpy)(pic)$_2$(H$_2$O)] (**1**) and [Ru^{II}(Eto-tpy)(pic)$_2$(H$_2$O)] (**2**).

This article is protected by copyright. All rights reserved

Author Manuscript

1864564x, 2022, 4, Downloaded from https://chemistry-europe.onlinelibrary.wiley.com/doi/10.1002/cssc.202101657 by Office Of Scientific And Technical Information, Wiley Online Library on [28/09/2023]. See the Terms and Conditions (https://onlinelibrary.wiley.com/terms-and-conditions) on Wiley Online Library for rules of use; OA articles are governed by the applicable Creative Commons License

Results and discussion

Samples preparation and characterization

$[Ru^{II}(R\text{-}tpy)(pic)_2(Cl)]Cl$ complexes were prepared by reacting two equivalents of pic ligand with the precursor complex $[Ru(R\text{-}tpy)Cl_3]$ (**Scheme 1**). The $[Ru^{II}(R\text{-}tpy)(pic)_2(H_2O)](NO_3)_2$ complexes **1** and **2** were prepared from a solution of $[Ru^{II}(R\text{-}tpy)(pic)_2(Cl)]Cl$ in water with the addition of 2 equivalents of $AgNO_3$, followed by stirring for 12 hours at room temperature. The ^{1}H-NMR, ^{13}C-NMR and high resolution mass spectroscopy of the prepared complexes are provided in (**Figures S1-S12)**.

Uv-vis spectra of **1** and **2** in water are shown in (**Figure 2)**. The peaks at 508 and 468 nm can be assigned to the Metal-to-Ligand charge transfer, and the peaks at 354, 307, and 270 nm represent the Ligand-to-Metal charge transfer in complex **1**. The peaks at 516 and 476 nm can be assigned to the Metal-to-Ligand charge transfer, and the peaks at 358, 308, and 270 nm represent the Ligand-to-Metal charge transfer in complex **2**.

UV-Vis spectroscopy was used to monitor absorption changes with the consecutive addition (titration) of CAN to the catalyst in 0.1 M HNO_3 solution (**Figures S13-S16**). With addition of 1 equiv. of CAN to the 0.5 mM $[Ru^{II}(R\text{-}tpy)(pic)_2(H_2O)]^{2+}$, the intensity of the band in the visible region decreased, consistent with the generation of the $[Ru^{III}(R\text{-}tpy)(pic)_2(H_2O)]^{3+}$. Further addition of another 1 equiv. of CAN resulted in a further decrease in the peak intensity, consistent with the generation of a $[Ru^{IV}{=}O]^{2+}$ species. After addition of 2 equiv. of CAN, no substantial changes were observed in the spectral bands in visible region complexes **1** and **2**, respectively.

This article is protected by copyright. All rights reserved

Author Manuscript

1864564x, 2022, 4, Downloaded from https://chemistry-europe.onlinelibrary.wiley.com/doi/10.1002/cssc.202101657 by Office Of Scientific And Technical Information, Wiley Online Library on [28/09/2023]. See the Terms and Conditions (https://onlinelibrary.wiley.com/terms-and-conditions) on Wiley Online Library for rules of use; OA articles are governed by the applicable Creative Commons License

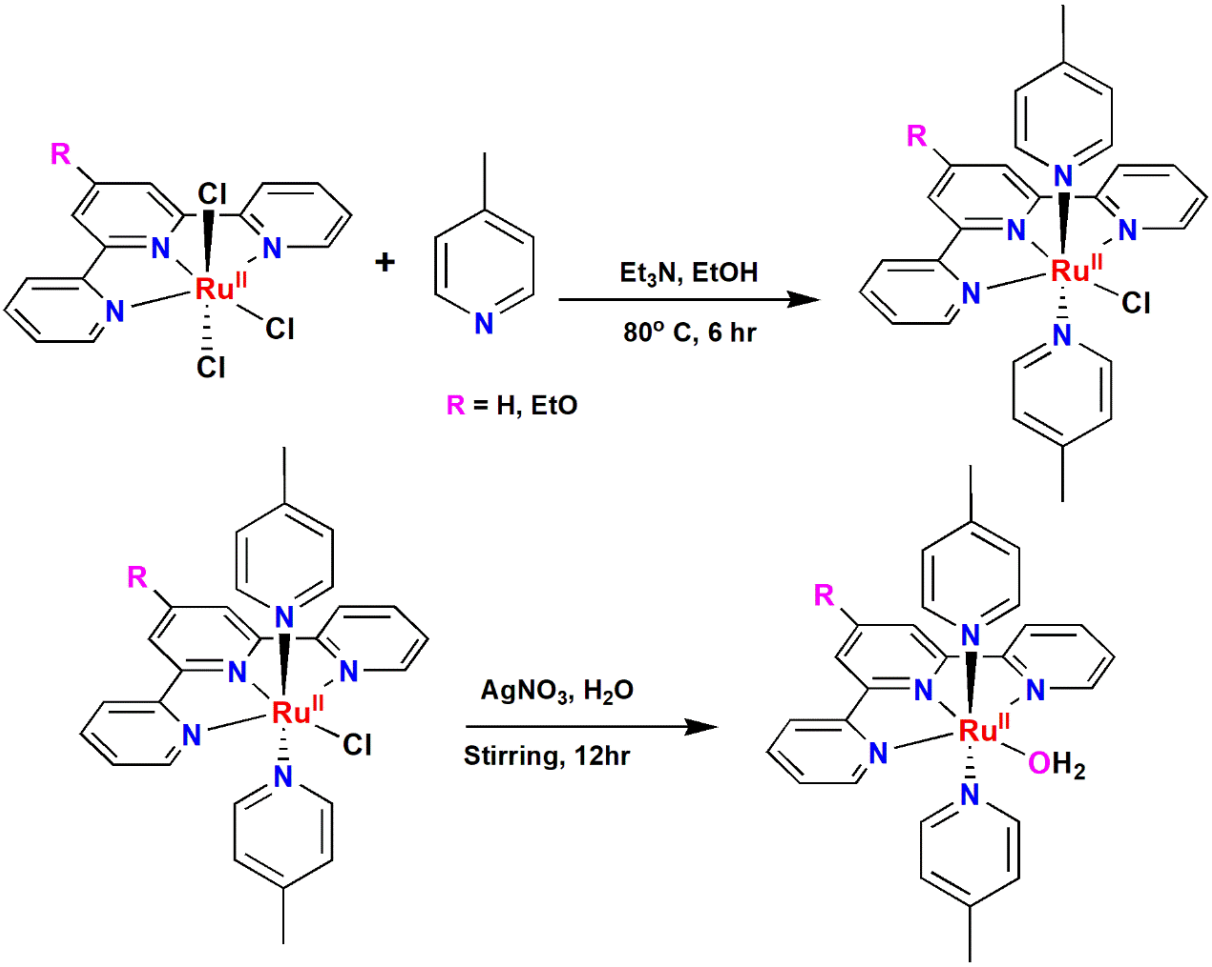

Scheme 1. Preparation of complexes

Aqueous Electrochemistry

The electrochemical studies of both complexes were performed with 0.5 mM solutions of the catalyst in 0.1 M HNO_3 (**Figures 3, S17-24**). Using CV, the Ru^{II}/Ru^{III} reversible redox couple was observed at 0.80 V and 0.77 V vs. Ag/AgCl for complexes **1** and **2,** respectively (**Figures 3, S17, S18**). We did not observe separate redox processes for the Ru^{III}/Ru^{IV} couple at pH = 1. It was reported in the literature that separate redox processes for the Ru^{III}/Ru^{IV} couple at pH = 1 are not always observed [57, 69] as the potentials for both Ru^{II}/Ru^{III} and Ru^{III}/Ru^{IV} redox couples are very close. Additionally, electrochemical waves have considerable widths of ~200 mV, and some waves have extended plateaus which makes it difficult to find maximum points. It also can be that Ru^{II}-to-Ru^{III} transition is not well pronounced at pH=1 but rather that the Ru^{III}-to-Ru^{IV} transition dominates, masking the position of the Ru^{II}-to-Ru^{III} couple, predicted by DFT to be close to ~0.7 V. Further electrochemical study was carried out at pH = 6.5 (**Figures S19-S24**). The redox couples for Ru^{II}/Ru^{III}, Ru^{III}/Ru^{IV} were observed at 0.28 V and 0.56 V vs. Ag/AgCl for **1** (**Figures S20, S22**) and 0.22 V and 0.50 V vs. Ag/AgCl for **2** (**Figures S21, S23**). These results indicate that both redox processes are proton-coupled electron transfer

This article is protected by copyright. All rights reserved

Author Manuscript

1864564x, 2022, 4, Downloaded from https://chemistry-europe.onlinelibrary.wiley.com/doi/10.1002/cssc.202101657 by Office Of Scientific And Technical Information, Wiley Online Library on [28/09/2023]. See the Terms and Conditions (https://onlinelibrary.wiley.com/terms-and-conditions) on Wiley Online Library for rules of use; OA articles are governed by the applicable Creative Commons License

(PCET). The first process is likely Ru^{II}-H_2O to Ru^{III}-OH PCET oxidation, while the second might be Ru^{III}-OH to Ru^{IV}=O PCET. From 0.8 V at pH=1, $1e^-/1H^+$ PCET is expected to shift the electrochemical wave to 0.475 V, which differs from the 0.28 V observed at pH=7 by 0.195 V. Thus, if both numbers have ±100 mV uncertainty shift from side of the peak, ~0.7 V to 0.375 V makes the expected number to fall within 100 mV of the reported 0.28 V. The onset of catalytic current was detected at ~1.55 V and ~1.46 V vs. Ag/AgCl for **1** and **2**, respectively, indicating the electrocatalysis of water oxidation (**Figures 3, S24**).

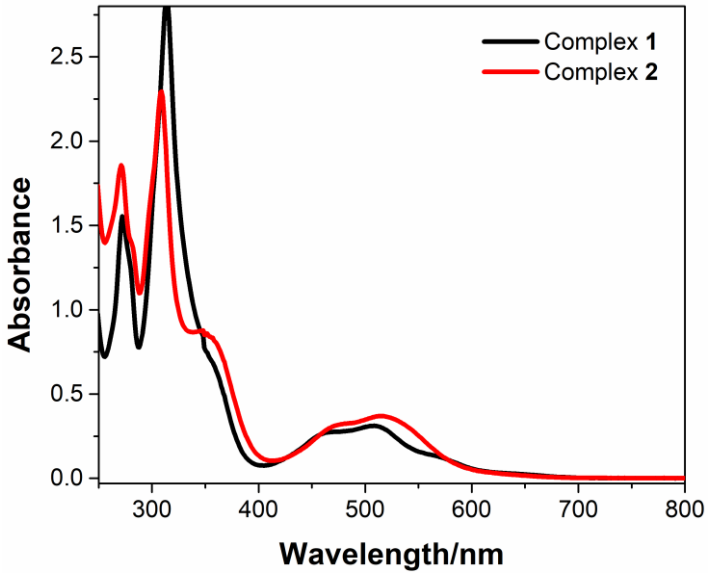

Figure 2. UV-visible spectra of complex **1** and **2** in water (conc. = 0.75 mM, path length = 1 mm).

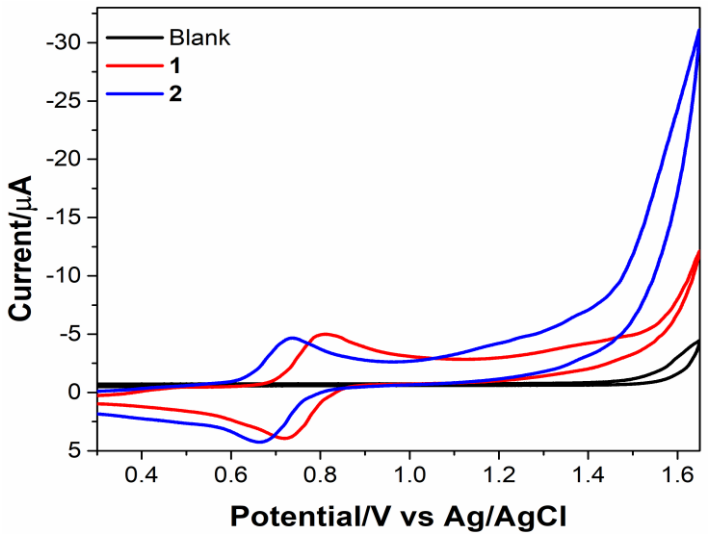

Figure 3. CV of 0.5 mM **1** (red) and **2** (blue) with catalytic current and CV of blank (black), pH = 1 (0.1 M HNO_3).

Chemical O_2 Evolution

This article is protected by copyright. All rights reserved

1864564x, 2022, 4, Downloaded from https://chemistry-europe.onlinelibrary.wiley.com/doi/10.1002/cssc.202101657 by Office Of Scientific And Technical Information, Wiley Online Library on [28/09/2023]. See the Terms and Conditions (https://onlinelibrary.wiley.com/terms-and-conditions) on Wiley Online Library for rules of use; OA articles are governed by the applicable Creative Commons License

Author Manuscript

The catalytic water oxidation of **1** and **2** was carried out at pH=1 (0.1 M HNO_3) using CAN as oxidant, (**Figures 4, S25-S40)**. The number of moles of O_2 was recorded by a Clark electrode in aerobic conditions. To determine the rate law for O_2 evolution, two series of experiments were conducted. First, the concentration of catalyst was varied from 0.1 mM to 0.5 mM while keeping the CAN concentration constant (20 mM). The evolution rate of O_2 increases with increasing the catalyst concentration (**Figure 4(a)**). The kinetics of O_2 evolution were determined by considering the rate of O_2 evolution from the linear regime of [O_2] increase (~10 sec after the addition of oxidant) at different concentration of catalyst (**Figure S25**). This showed that the rate of O_2 evolution is 1st order with the respect to the concentration of **2** (k^{CAN}_{obs} = 31.6 μM s^{-1}, where k^{CAN}_{obs} is a O_2 evolution rate at constant, 20 mM CAN concentration) (**Figure S26**). Similarly, **1** showed 1st-order kinetics with k^{CAN}_{obs} = 15.9 μM s^{-1}, (**Figures S27-S29**). According to the rate constant the compound **2** is ~2 times more active than compound **1** at 0.5 mM concentration.

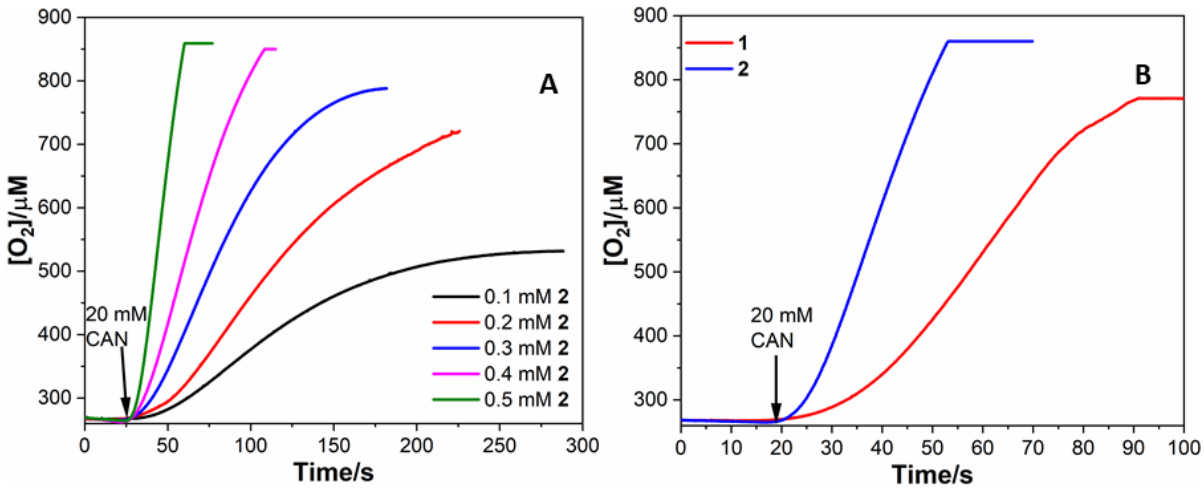

Figure 4. (a) O_2 evolution at different concentrations of **2** in 0.1 M HNO_3, 20 mM of CAN added at t = 25 sec. (b) Comparison of O_2 evolution for both **1** and **2** (0.5 mM) in 0.1 M HNO_3, 20 equiv. of CAN added at t = 18 sec.

In the second series of experiments (**Figures S30-S35**), the concentration of the catalyst was kept constant (0.5 mM) while the concentration of CAN was varied from 10 mM to 40 mM. The rate of O_2 evolution increases with increasing concentration of CAN (**Figures S30, S33**), and the rate was determined by considering the initial rate of O_2 evolution (~5 sec after the addition of oxidant) at different concentrations of CAN (**Figures S31, S34**). (**Figures S32** and **S35)** show that the initial rate of O_2 evolution is 1st order with respect to the CAN concentration for both catalysts, and the obtained rate constants were k^{Ru}_{obs} = 0.18 μM s^{-1} (where k^{Ru}_{obs} is a

This article is protected by copyright. All rights reserved

Author Manuscript

1864564x, 2022, 4, Downloaded from https://chemistry-europe.onlinelibrary.wiley.com/doi/10.1002/cssc.202101657 by Office Of Scientific And Technical Information, Wiley Online Library on [28/09/2023]. See the Terms and Conditions (https://onlinelibrary.wiley.com/terms-and-conditions) on Wiley Online Library for rules of use; OA articles are governed by the applicable Creative Commons License

O_2 evolution rate at constant, 0.5 mM Ru catalyst concentration) and 0.43 µM s^{-1} for **1** and **2,** respectively. For both complexes, we compared the activity of oxygen evolution at a 0.5 mM concentration of **1** and **2**. Catalyst **2** shows ~2 times higher catalytic activity (**Figure 4(b)**).

For kinetic analysis, the linear section of the O_2 evolution curve was used. Notably, this excludes the preceding lag phase (**Table S1)**. Very prominent lag phases were reported for a class of Ru-based WOCs with quaterpyridine ligands.[70-73] This lag phase was convincingly assigned to the formation of N-oxides of the quaterpyridine ligands, ensuring onset of catalytic activity.[73] Smaller lag phases of 20-100 sec were measured for $[Ru(EtO\text{-}tpy)(bpy)(H_2O)]^{2+}$ and $[Ru(tpy)(bpy)(H_2O)]^{2+}$, correspondingly, and these were assigned to the formation of complexes with N-oxide ligands, such as tpy- and bpy- N-oxides, based on the ~835 cm^{-1} Raman signature sensitive to $^{16}O/^{18}O$ exchange.[57] Here, we recorded smaller lag phases of ~8 to ~0 sec for **1** and **2,** correspondingly, and we did not observe vibrations typical of Ru complexes with N-oxide ligands (see resonance Raman section below). Thus, we concluded that **2** is an active catalyst in its native ligand environment, and it does not require oxidative ligand modification to gain catalytic activity.

Table 1 Comparison of O_2 evolution rates for structurally similar catalysts.

Catalyst	Ligand Effect	Catalytic Conditions	Rate [a] of O_2 evolution (µM s^{-1})	Reference
$[Ru^{II}(EtO\text{-}tpy)(pic)_2(H_2O)]$	ED	pH = 1 HNO_3	31.6	In this paper
$[Ru^{II}(tpy)(pic)_2(H_2O)]$	-	pH = 1 HNO_3	15.9	In this paper
$[Ru^{II}(EtO\text{-}tpy)(bpy)(H_2O)]$	ED	pH = 1 HNO_3	1.8	[57]
$[Ru^{II}(tpy)(bpy\text{-}NO)(H_2O)]$	ED	pH =1 HNO_3	10	[57]
$[Ru^{II}(tpy)(bpy)\ (H_2O)]$	-	pH = 1 HNO_3	0.34	[56]
$[Ru^{II}(MeO\text{-}tpy)(bpy)(H_2O)]$	ED	pH = 1	2.4	[56]
$[Ru^{II}(Me\text{-}tpy)(bpy)(H_2O)]$	ED	pH = 1	0.61	[56]
$[Ru^{II}(Cl\text{-}tpy)(bpy)(H_2O)]$	EWD	pH = 1	0.43	[56]
$[Ru^{II}(2py\text{-}tpy)(bpy)(H_2O)]$	EWD	pH = 1 Triflic acid	1.19	[12]
$[Ru^{II}(3py\text{-}tpy)(bpy)(H_2O)]$	EWD	pH = 1 Triflic acid	0.96	[12]
$[Ru^{II}(4py\text{-}tpy)(bpy)(H_2O)]$	EWD	pH = 1 Triflic acid	1.23	[12]

This article is protected by copyright. All rights reserved

Author Manuscript

1864564x, 2022, 4, Downloaded from https://chemistry-europe.onlinelibrary.wiley.com/doi/10.1002/cssc.202101657 by Office Of Scientific And Technical Information, Wiley Online Library on [28/09/2023]. See the Terms and Conditions (https://onlinelibrary.wiley.com/terms-and-conditions) on Wiley Online Library for rules of use; OA articles are governed by the applicable Creative Commons License

$[Ru^{II}(Ql\text{-}tpy)(bpy)(H_2O)]$	EWD	pH = 1 Triflic acid	0.75	[13]
$[Ru^{II}(QCl\text{-}tpy)(bpy)(H_2O)]$	ED	pH = 1 Triflic acid	0.78	[14]

ED = Electron donating group, EWD = Electron withdrawing group, [a] rate is reported for the following experimental condition: concentration of the catalyst is 1 mM and CAN is 20 mM.

Photochemical O_2 Evolution

The photochemical water oxidation experiments were conducted at 20 ^oC, in a 0.1 M phosphate buffer solution at pH ≈ 7 by employing a three component system containing photosensitizer ($[Ru(bpy)_3]Cl_2$), sacrificial electron acceptor ($Na_2S_2O_8$), and the catalyst ($[Ru(R\text{-}tpy)(pic)_2((H_2O)](NO_3)_2$ (**1** and **2**) with a visible light (LED; visible light 60 W). The evolved O_2 was measured with the Clark electrode.

Various controlled experiments were conducted by considering all three components. Under catalytic conditions in absence of the photosensitizer and light, the system contained only the catalyst and the sacrificial electron acceptor $Na_2S_2O_8$; here, a negligible amount of O_2 was measured (**Figure 5**), which reveals that the presence light and a photosensitizer play a crucial role in photocatalytic water oxidation in a three-component system. For the photocatalytic system comprising of the photosensitizer and the sacrificial electron acceptor, a very minor amount of evolution was observed, but the rate was very slow as compared to the catalytic system in the presence of all three components (**Figure 5**).

The system containing $[Ru(bpy)_3]Cl_2$ (1 x 10^{-3}M), catalyst $[Ru(R\text{-}tpy)(pic)_2(H_2O)]^{2+}$ (25μM to 100 μM), and $Na_2S_2O_8$ (1 x 10^{-2}M) was irradiated with the visible light source. The system showed a significant evolution of O_2 (**Figures 5, S36-S41**) due to the photocatalytic water oxidation. The kinetics were determined by considering the initial rate of evolution, which shows that the rates of O_2 evolution at different complex concentrations (**1** and **2**) were first order having $k^{h\nu}_{obs}$ = 38 μM s^{-1} (where $k^{h\nu}_{obs}$ is a O_2 evolution rate under photochemical conditions with 1 x 10^{-3} M $Ru(bpy)_3]Cl_2$ and 1 x 10^{-2} M $Na_2S_2O_8$) and 61 μM s^{-1}, respectively (**Figures S38 and S41**). For both complexes, we compared the activity of oxygen evolution at a 100 μM concentration of **1** and **2**. Catalyst **2** shows ~2 times higher photocatalytic activity; we conclude that **2** is more active towards photocatalytic activity.

This article is protected by copyright. All rights reserved

1864564x, 2022, 4, Downloaded from https://chemistry-europe.onlinelibrary.wiley.com/doi/10.1002/cssc.202101657 by Office Of Scientific And Technical Information, Wiley Online Library on [28/09/2023]. See the Terms and Conditions (https://onlinelibrary.wiley.com/terms-and-conditions) on Wiley Online Library for rules of use; OA articles are governed by the applicable Creative Commons License

Author Manuscript

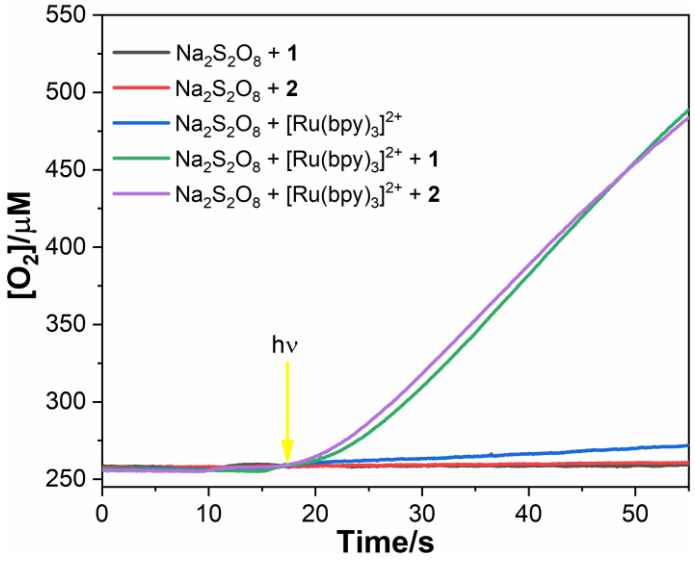

Figure 5. Photochemical O_2 evolution in 0.1 M phosphate buffer (pH=7, 0.5 mL) of: $Na_2S_2O_8$ (0.1 M) and catalyst **1** (100 μM), black curve; $Na_2S_2O_8$ (0.1 M) and catalyst **2** (100 μM), red curve; $Na_2S_2O_8$ (0.1 M) $[Ru(bpy)_3]Cl_2$ (1 mM), blue curve; $Na_2S_2O_8$ (0.1 M), $[Ru(bpy)_3]Cl_2$ (1 mM), catalyst **1** and **2**, blue and pink curves, respectively.

EPR Spectroscopy

Cryogenic EPR spectroscopy was used to identify the active paramagnetic intermediates involved in the catalysis. Initial **1** and **2** are diamagnetic, as they contain low-spin Ru^{II} (d^6, S = 0). **1** and **2** were oxidised by the addition of different equivalents of CAN, and samples were frozen within 30s after mixing. The EPR of **1** and **2** with addition of 1, 2, 3, and 20 equiv. of CAN are shown in (**Figures 6(a,b), S41, S43)**. Previously, we showed that substitution with the EtO-tpy ligand in $[Ru(tpy)(bpy)(H_2O)]^{3+}$ results in a g-tensor with larger anisotropy.[57] Here, we observe a similar trend with **2** displaying a more anisotropic EPR signal, (**Figure 6(b))**. That the EPR spectra of **1** and **2** tend to be axial and rhombic, respectively, proves unsurprising. DFT calculations predict asymmetries in the EtO ligand in **2;** this combined with the electron-donating tendency of this ligand motivates the presence of rhombic spectra, whereas spectra resulting from intermediates of the more symmetric **2** are axial.

Upon addition of 1 equiv. of CAN to **1,** the maximum intensity of S = ½ axial signal ($g_{\|} \sim 2.49$ and $g_{\perp} \sim 1.55$), corresponding to the Ru^{III} state, was observed. Addition of higher amounts (2, 3, and 20 equiv.) of CAN resulted in the decrease of the Ru^{III} signal, consistent with the formation of the $[Ru^{IV}{=}O(tpy)(pic)_2]^{2+}$ (S = 1) species, which is EPR silent, (**Figure S42)**.[74] A more complex dependence is detected for **2** where the EPR signal consistent with Ru^{III} state ($g_{xx} \sim 2.62$ and $g_{yy} \sim 2.3$, position of g_{zz} is not resolved) is present in samples produced by

This article is protected by copyright. All rights reserved

Author Manuscript

1864564x, 2022, 4, Downloaded from https://chemistry-europe.onlinelibrary.wiley.com/doi/10.1002/cssc.202101657 by Office Of Scientific And Technical Information, Wiley Online Library on [28/09/2023]. See the Terms and Conditions (https://onlinelibrary.wiley.com/terms-and-conditions) on Wiley Online Library for rules of use; OA articles are governed by the applicable Creative Commons License

addition of 1, 2, or 3 equiv. CAN, (**Figure 6(b))**. This signal disappears when **2** is oxidized with excess (+20 equiv.) of CAN.

To analyse the stability of EPR signals, all the samples were melted at room temperature for 2 minutes, then refrozen and re-measured. With 1, 2, and 3 equiv. CAN added, 2 minutes of melting and refreezing leads to a small change in the signal, (**Figure S42)**. This suggests a mixture of Ru^{III} and Ru^{II} (EPR silent) states are formed when **2** is quickly mixed with few CAN equivalents. Upon melting, Ru^{II} continues to react with CAN, resulting in an increase in the Ru^{III} signal. After addition of 20 equiv. of CAN, the Ru^{3+} signal with $g_{xx} \sim 2.62$ and $g_{yy} \sim 2.3$ is no longer detectable, indicating full oxidation past this state and later reactivity forming a new signal with ($g_{xx} = 2.17$ and $g_{yy} = 2.07$). The power dependence of this signal is shown in (**Figure S44).** This power dependence is consistent with that of a transition metal-based paramagnetic species, as no saturation can be achieved using maximum available microwave power. Melting of the +20 equiv. sample results in small return of the EPR intensity at $g_{xx} \sim 2.62$ and $g_{yy} \sim 2.3$, indicating the turn on of the catalytic system, (**Figure S42)**.

This article is protected by copyright. All rights reserved

Author Manuscript

1864564x, 2022, 4, Downloaded from https://chemistry-europe.onlinelibrary.wiley.com/doi/10.1002/cssc.202101657 by Office Of Scientific And Technical Information, Wiley Online Library on [28/09/2023]. See the Terms and Conditions (https://onlinelibrary.wiley.com/terms-and-conditions) on Wiley Online Library for rules of use; OA articles are governed by the applicable Creative Commons License

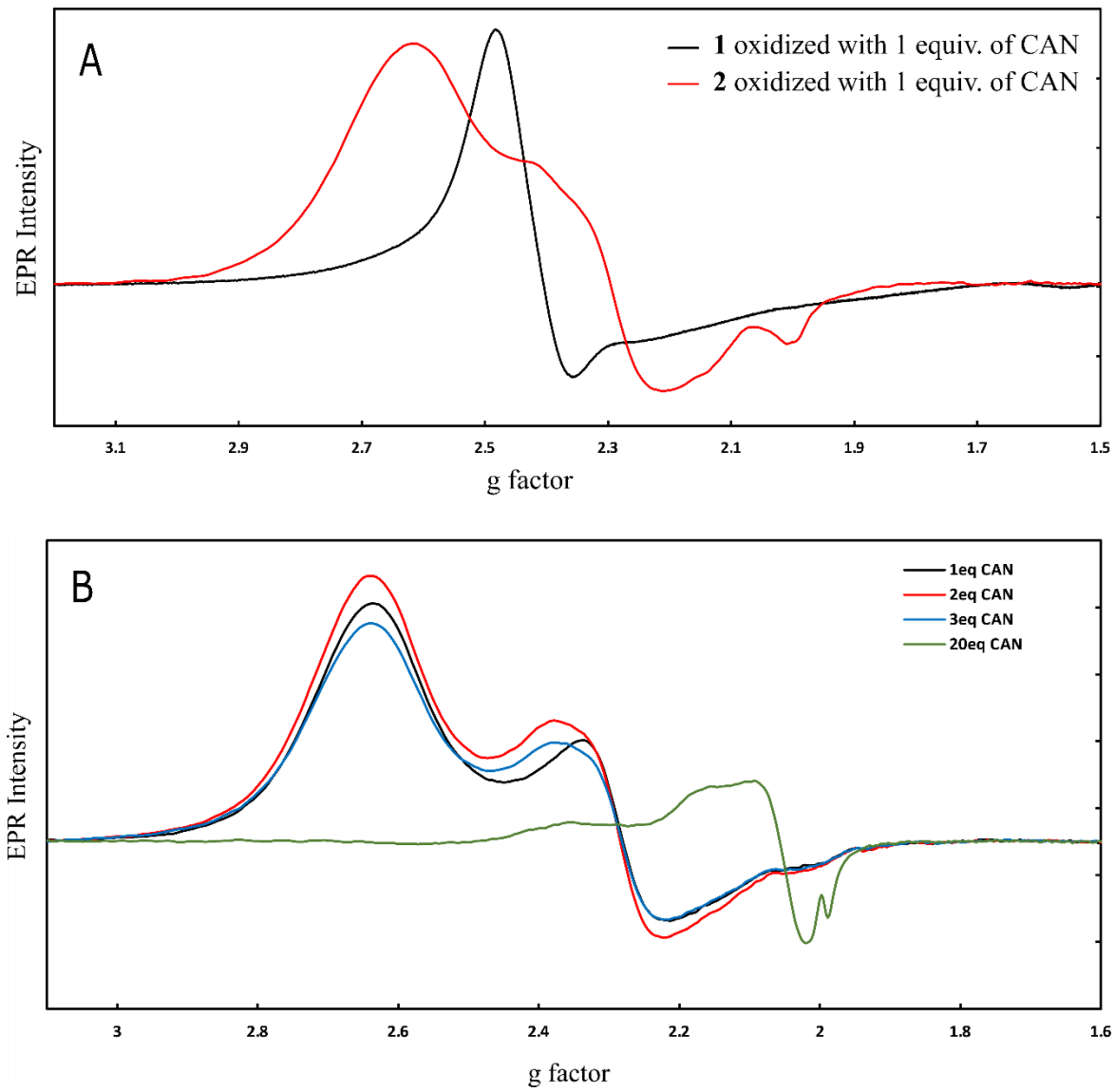

Figure 6. A) EPR spectra (20 K) of 1 mM of **1** and **2**, in 0.1 M HNO_3 after addition of 1 equiv. of CAN and immediate freezing of the sample. Y-axis is adjusted for optimal comparison of signals. B) EPR spectra (20K) of samples quickly frozen after addition of 1, 2, 3, and 20 equiv. CAN to 1 mM **2** in 0.1 M HNO_3.

Assignment of the new g_{xx} = 2.17 / g_{yy} = 2.07 EPR signal is non-trivial. One potential interpretation of the signal near g-factor 2.07 is assignment to the highly reactive Ru^V intermediate, (**Table S2).** However, all reported Ru^V EPR spectra have a characteristic g_{zz} component of the g-tensor, which is notably absent in EPR spectra of **2** with excess (20 equiv.) CAN, (**Figure 6(b)**). Melting the sample for 2 minutes reveals relative stability of the g_{xx} = 2.17 / g_{yy} = 2.07 EPR signal, unlikely for the Ru^V state of such highly active catalyst. Dimer formation might result in new EPR signals. The blue dimer [III,IV] state has g-factor below ~2 , and the [IV,V] state has peak at ~2.03.[75] However, EXAFS analysis did not detect dimer species in same samples. We tentatively assign this new EPR signal to a complex of superoxide

This article is protected by copyright. All rights reserved

Author Manuscript

1864564x, 2022, 4, Downloaded from https://chemistry-europe.onlinelibrary.wiley.com/doi/10.1002/cssc.202101657 by Office Of Scientific And Technical Information, Wiley Online Library on [28/09/2023]. See the Terms and Conditions (https://onlinelibrary.wiley.com/terms-and-conditions) on Wiley Online Library for rules of use; OA articles are governed by the applicable Creative Commons License

with Ru species. We cannot also exclude this signal to be a Ru^{III}-OOH species as, to the best of our knowledge, EPR of such species has not been reported.

X-ray absorption spectroscopy

The results of Ru K-edge XANES and EXAFS analysis of initial **2** and **2** under water oxidation catalysis initiated by addition of 20 equiv. of CAN are shown in (**Figures 7 and S44)**.

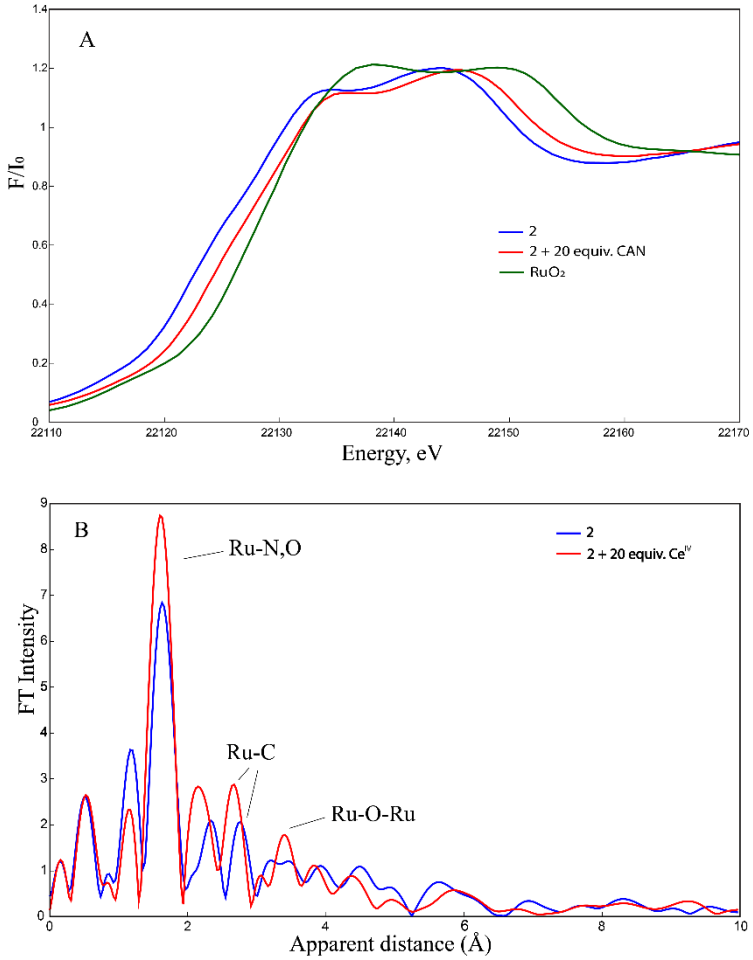

Figure 7. Ru K-edge XAS at 20 K. A) XANES of **2** (blue), with addition of 20 equiv. of CAN to **2** (red) and of Ru^{IV} oxide (green). B) Fourier transforms of k^3 -weighted Ru EXAFS of **2** before (blue) and after addition of 20 equiv. of CAN (red) in 0.1 M HNO_3 solution.

XANES data agree with the Ru^{II} oxidation state in initial **2**. However, samples of **2** quickly frozen after addition of 20 equiv. of CAN appear to have a mixture of the Ru^{III} (or Ru^{II}) and Ru^{IV} oxidation states. The Ru K-edge is shifted to lower energy compared to the RuO_2 reference, (**Figure 7A)**. This agrees with EPR results, indicating that sample is paramagnetic. (**Figure 7B)** compares Fourier transforms of Ru EXAFS of **2** before and after addition of 20 equiv. of CAN. (**Table S3)** and **(Figure S46)** show results of the EXAFS fits of the initial compound **2**. EXAFS fits predict five Ru−N interactions at ~ 2.08 Å in the first coordination

This article is protected by copyright. All rights reserved

Author Manuscript

1864564x, 2022, 4, Downloaded from https://chemistry-europe.onlinelibrary.wiley.com/doi/10.1002/cssc.202101657 by Office Of Scientific And Technical Information, Wiley Online Library on [28/09/2023]. See the Terms and Conditions (https://onlinelibrary.wiley.com/terms-and-conditions) on Wiley Online Library for rules of use; OA articles are governed by the applicable Creative Commons License

sphere as well as ten Ru−C distances at ~2.9-3.1 Å in the second coordination sphere, (**Table S3)**. It is unclear whether water is bound to the Ru center in the acidic solution (0.1 M HNO_3) of the initial compound. Attempts to fit a sixth oxygen ligand resulted in the fit with Ru-O distance ~2.6 Å, which is too long for the direct ligand, (**Table S3).** DFT predicts water binding to Ru in **2** with negative ΔG, (**Table 2)**. (**Table S4)** and **(Figure S47)** show results of the EXAFS fits of species formed upon addition of 20 equiv. CAN to **2.** While overall complex architecture remains preserved upon oxidation, such as Ru-N/O first and Ru-C second coordination spheres are similar to initial compound, we were unable to fit specific structural elements of the oxidized species such as Ru^{IV}=O distance or Ru-OO peroxo fragment. This is likely due to the mixture of several species in the sample.

The included EXAFS/XANES data (**Figures 7, S43, S44, S45; Tables S3, S4**). Are in good agreement with geometries predicted in DFT computation. For example, the structural parameters for the EXAFS fits of initial **2**, shown in Table S3, coincide nicely with the geometry computed for non H_2O-coordinated **2.** EXAFS fits predict coordination spheres, in Angstroms, of (Ru-N: 2.08; Ru-C_{inner}: 2.91; and Ru-C_{outer}: 3.08); DFT geometries for the **2** predict coordination spheres, in Angstroms, of (Ru-N: 2.11; Ru-C_{inner}: 2.92; and Ru-C_{outer}: 3.11). Further, while fits were attempted on **2** oxidized by 20 equiv. of CAN, this was made highly difficult due to the multi-species mixture of states. This is consistent with EPR data (Figures 6, S32), wherein melting of intermediates resulting in a slightly reduced signal of Ru^{III} features suggest relative stability of the intermediate, as well as a mixture of EPR-silent Ru^{II}/Ru^{IV} states. The melting of **2** plus 20 equiv. of CAN resulting in a re-emergence of the g_{xx} ~ 2.62 and g_{yy} ~ 2.3 feature (assigned to Ru^{III}), further suggests the presence of a mixture of states: Ru^{III}, Ru-peroxo, and some EPR-silent $Ru^{II/IV}$ states. That resonance Raman experiment (see below) detects the Ru^{IV}=O intermediate despite a mixture of states is unsurprising. The Ru^{IV}=O vibrational mode has been well characterized and is a highly Raman-active feature. Some of the species predicted by the proposed mechanism – Ru^{II}-H_2O, Ru^{III}-H_2O, Ru^{III}-OH – are likely to have far weaker Ru-O vibrations than Ru^{IV}=O. Thus, even that Ru^{IV}=O is present in Raman, the mixture of states obscures its presence in EXAFS fitting and XANES spectra.

Raman

Resonance Raman was performed on the complex **2** to study intermediates formed after addition of CAN. Spectra of initial **2** in $H_2{}^{16}O$ and $H_2{}^{18}O$ are shown in **(Figure S48)**. Upon addition of 20 equiv. of CAN a peak at 778 cm^{-1} appears (**Figure 8(a)**), which is typical of

This article is protected by copyright. All rights reserved

Author Manuscript

1864564x, 2022, 4, Downloaded from https://chemistry-europe.onlinelibrary.wiley.com/doi/10.1002/cssc.202101657 by Office Of Scientific And Technical Information, Wiley Online Library on [28/09/2023]. See the Terms and Conditions (https://onlinelibrary.wiley.com/terms-and-conditions) on Wiley Online Library for rules of use; OA articles are governed by the applicable Creative Commons License

Ru^{IV}=O vibrations. We reported similar Ru^{IV}=O vibrations for $[Ru^{IV}=O(tpy)(bpy)]^{2+}$ and $[Ru^{IV}=O(EtO\text{-}tpy)(bpy)]^{2}$ intermediates.[57] When the same reaction is conducted in $H_2{}^{18}O$, this peak shifts -36 cm^{-1}, in agreement with the DFT-predicted -38 cm^{-1} shift (**Figure S49(a)**). Thus, the 778 cm^{-1} is assigned to Ru^{IV}=O. There is one more oxygen sensitive band at 823 cm^{-1} for which the exact ^{18}O shift is difficult to estimate due to overlapping bands; the shift is estimated in the 40-58 cm^{-1} range. The peak at 832 cm^{-1} is similar to Ru-O-N vibrations of Ru-coordinated N-oxide ligands that we previously reported[76-78], but the ^{18}O isotope shift is greater than previously observed for Ru-O-N vibrations of Ru-coordinated N-oxide ligands. The ^{18}O isotope shift exceeding 40 cm^{-1} might indicate a presence of the O-O vibration. Thus, analysis of the reaction mixture in 50%-50% $H_2{}^{18}O$-$H_2{}^{16}O$ was conducted, (**Figures 8(b,c))**. In these conditions additional peak at ~800 cm^{-1} is observed which is ~ 2 times more intense than 823 cm^{-1} peak. This is a well-known feature of O-O bond arising from the partially labelled ^{16}O-^{18}O fragment. From this feature, we can conclude that ^{18}O isotope shift for 823 cm^{-1} band is ~46 cm^{-1}, which falls in the 40-58 cm^{-1} range estimated above (**Figure 8(a))**.

Single point DFT calculations on previously optimized geometries may simulate Raman spectra, as is shown for select intermediates in the **2** catalytic system, (**Figure S49)**. Images of vibrational modes discussed are shown in **(Figure S50).** The simulated Raman spectrum of the $[Ru^{IV}=O(EtoTpy)(4\text{-}pic)_2]^{2+}$ state reveals a strong Ru-O vibration at 784 cm^{-1}. Furthermore, with ^{18}O substitution, the isotope shift of this Ru^{IV}=O peak is computed to be -38 cm^{-1}. This supports assignment of the experimentally observed 778 cm^{-1} peak to the Ru^{IV}=O intermediate (**Figure S49(a))**. Computed Raman spectra of peroxide species $[Ru^{IV}\text{-}OO(EtO\text{-}tpy)(4\text{-}pic)_2]^{3+}$ and $[Ru^{III}\text{-}OOH(EtO\text{-}tpy)(4\text{-}pic)_2]^{2+}$ reveal Ru-OO vibrations near 1400 cm^{-1} and 880 cm^{-1}, respectively (**Figures S49(b,c))**. Isotope shifts of these intermediates' vibrations were -82 cm^{-1} and -44.5-53.5 cm^{-1}, respectively. This suggests a possible assignment of the experimentally observed 823 cm^{-1} peak to the Ru^{III}-OOH peroxide intermediate (**Figure S49(b))**. This also implies a mixture of Ru^{IV}=O and Ru^{III} states in samples produced by addition of the 20 equiv. CAN and fast freezing which agrees with EPR and XAS data.

This article is protected by copyright. All rights reserved

Author Manuscript

1864564x, 2022, 4, Downloaded from https://chemistry-europe.onlinelibrary.wiley.com/doi/10.1002/cssc.202101657 by Office Of Scientific And Technical Information, Wiley Online Library on [28/09/2023]. See the Terms and Conditions (https://onlinelibrary.wiley.com/terms-and-conditions) on Wiley Online Library for rules of use; OA articles are governed by the applicable Creative Commons License

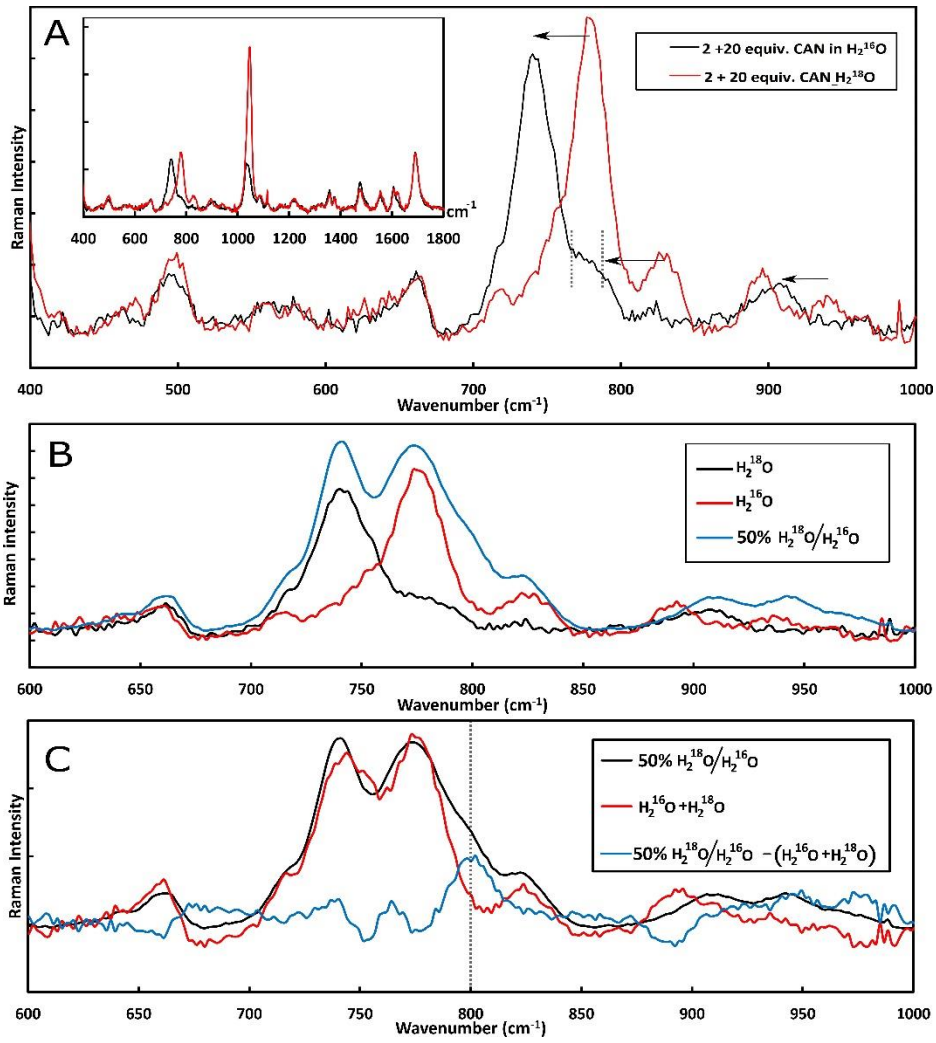

Figure 8. Resonance Raman spectra of **2** in $H_2{}^{18}O$ and $H_2{}^{16}O$ in 0.1 M HNO_3 after addition of 20 equiv. of CAN. The excitation wavelength is 442 nm. The experiment was conducted at cryogenic temperatures (liquid nitrogen) using cryostage.

DFT analysis of the mechanism

DFT was used to support the spectroscopic and catalytic activity analysis. Included are calculations of various proposed redox pathways and O-O bonding mechanisms, particularly the water nucleophilic attack pathways, (**Table 2, Figure 9)**. Calculated free energies of energy-optimized structures of intermediates of **1** and **2** are shown in (**Table S5)**. The selection of DFT parameters is consistent with the redox potentials of known Ru couples. Computed results for Ru^{II}/Ru^{III} and Ru^{III}/Ru^{IV} couples are within the generally accepted 200 mV range for DFT precision. From the oxygen evolution analysis, electrochemical studies, and spectroscopic results, we propose the reaction of **2** proceeds through one of three pathways, (**Scheme 2, Table 2)**. In the first, the initial $[Ru^{II}\text{-}(H_2O)]^{2+}$ species undergoes $1e^-$ oxidation, generating the $[Ru^{III}\text{-}(H_2O)]^{3+}$ species. This intermediate oxidises through PCET, generating the 6-coordinate $[Ru^{IV}\text{-}OH]^{3+}$ species which further oxidises to $[Ru^{V}{=}O]^{3+}$ at accessible ~+1.3 V potential. In

This article is protected by copyright. All rights reserved

Author Manuscript

1864564x, 2022, 4, Downloaded from https://chemistry-europe.onlinelibrary.wiley.com/doi/10.1002/cssc.202101657 by Office Of Scientific And Technical Information, Wiley Online Library on [28/09/2023]. See the Terms and Conditions (https://onlinelibrary.wiley.com/terms-and-conditions) on Wiley Online Library for rules of use; OA articles are governed by the applicable Creative Commons License

the second pathway, the initial $[Ru^{II}\text{-}(H_2O)]^{2+}$ species undergoes PCET, generating the $[Ru^{III}\text{-}OH]^{2+}$ species, which further oxidises through PCET to generate the $[Ru^{IV}{=}O]^{2+}$ species. The generated $[Ru^{IV}{=}O]^{2+}$ is protonated, forming the active $[Ru^{V}{=}O]^{3+}$ species via accessible PCET from the $[Ru^{IV}\text{-}OH]^{3+}$ intermediate. However, this step is predicted to be challenging due to the demanding ~+2.2 V potential. Alternatively, a third pathway is proposed wherein $[Ru^{IV}{=}O]^{2+}$ is oxidized directly to the high-valent $[Ru^{V}{=}O]^{3+}$ state; however, this step is predicted to be challenging due to the demanding ~+2.2 V potential. Note that $Ru^{V}{=}O$ intermediate was not detected by EPR, and if generated, it occurs in very low (below 0.5% of species) concentrations, though the high catalytic rate of catalysts **2** and **1** suggests that achieving high-valence Ru^{V} states possibly occurs in both catalysts. After achieving $Ru^{V}{=}O$, both pathways then undergo water nucleophilic attack (WNA) to generate the $[Ru^{III}\text{-}OOH]^{2+}$ intermediate, followed by either PCET step to generate the $[Ru^{IV}\text{-}OO]^{2+}$ species or via deprotonation to generate a Ru^{II} superoxo species; the $[Ru^{IV}\text{-}OO]^{2+}$ spin density is shown in **(Figure S51)**. Further water exchange with the $[Ru^{IV}\text{-}OO]^{2+}$ species releases O_2. Ru^{III}, $Ru^{IV}{=}O$, and one peroxo intermediate were detected spectroscopically.

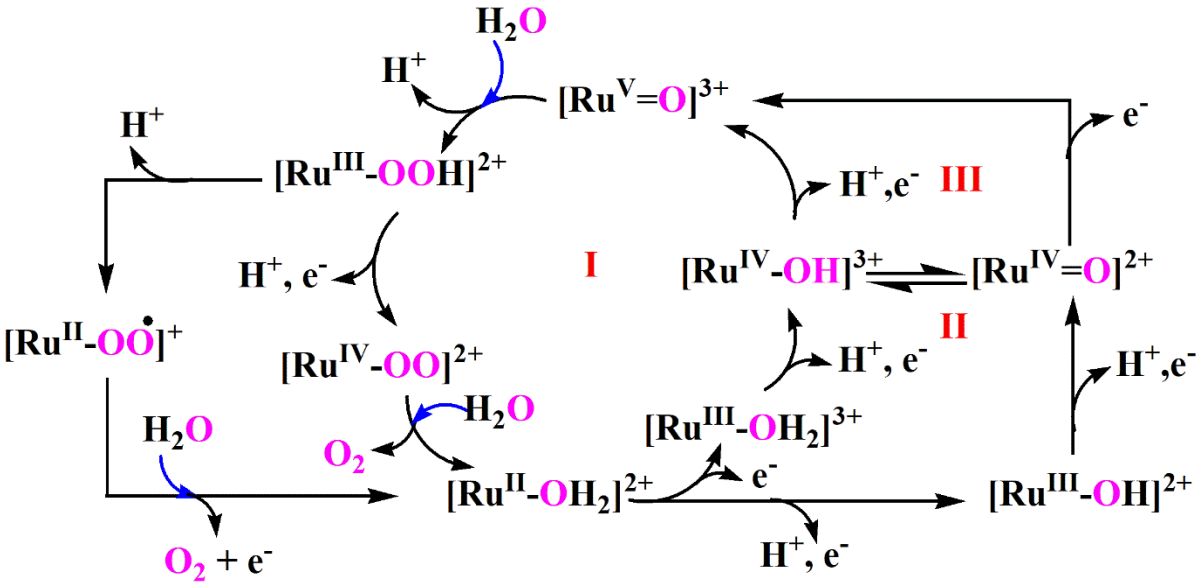

Scheme 2. Proposed mechanism for chemical water oxidation for $[Ru^{II}(EtO\text{-}tpy)(pic)_2(H_2O)]$ and $[Ru^{II}(tpy)(pic)_2(H_2O)]$ complexes.

Thus, considering the energetic differences between different Ru^{IV}-oxo species for both catalysts, a mixture of Ru^{IV}-oxo states likely occurs during oxidation of initial catalysts **2** and **1,** due to more facile formation of the Ru^{V} species from the Ru^{IV}-OH intermediates. From the Ru^{IV}-OH state, the Ru^{V} oxidation state is possible though use of sacrificial catalyst CAN (~1.7 V) or though electrolysis at a moderate potential. Note that the Ru^{V} state likely occurs in the

This article is protected by copyright. All rights reserved

1864564x, 2022, 4, Downloaded from https://chemistry-europe.onlinelibrary.wiley.com/doi/10.1002/cssc.202101657 by Office Of Scientific And Technical Information, Wiley Online Library on [28/09/2023]. See the Terms and Conditions (https://onlinelibrary.wiley.com/terms-and-conditions) on Wiley Online Library for rules of use; OA articles are governed by the applicable Creative Commons License

Author Manuscript

doublet state rather than quartet, as there is a ~0.1-0.2 eV energy difference in these spin states, depending on the catalyst (**Table S6**). The Ru^{IV}=O state has lower energy in the triplet spin state than in the singlet spin state, with a difference in thermal and electronic energies of +0.76 eV for both catalysts.

Water nucleophilic attack (WNA) pathways with peroxide formation were considered for both catalysts in the Ru^{IV}=O and Ru^{V}=O states. From the Ru^{IV}=O state, there are very high changes in free energies for both **1** and **2** reactions (+1.63 eV and +1.76 eV, respectively). This suggests that WNA is not feasible under normal catalytic conditions using CAN. However, if the high-valent Ru^{V}=O state is reached prior to WNA, the process becomes downhill (**1**: -0.74 eV, **2**: -0.60 eV). This suggests that O-O bond formation would be possible in the monomeric state, pending access to the high-valent Ru^{V} state. Following WNA on the Ru^{V}=O state, Ru^{II}-$OO^{\bullet -}$ superoxide formation via proton dissociation is predicted to be uphill for both catalysts (**1**: +0.37 eV, **2**: +0.43 eV), (**Table 2)**. The peroxide species may also undergo facile PCET oxidation to form $[Ru^{IV}\text{-}OO]^{2+}$ peroxide (**1**: +0.62 V, **2**: +0.68 V). The $[Ru^{IV}\text{-}OO]^{2+}$ peroxide structure was computed in singlet and triplet states with the triplet state ~0.4 eV lower in energy.

This article is protected by copyright. All rights reserved

Author Manuscript

1864564x, 2022, 4, Downloaded from https://chemistry-europe.onlinelibrary.wiley.com/doi/10.1002/cssc.202101657 by Office Of Scientific And Technical Information, Wiley Online Library on [28/09/2023]. See the Terms and Conditions (https://onlinelibrary.wiley.com/terms-and-conditions) on Wiley Online Library for rules of use; OA articles are governed by the applicable Creative Commons License

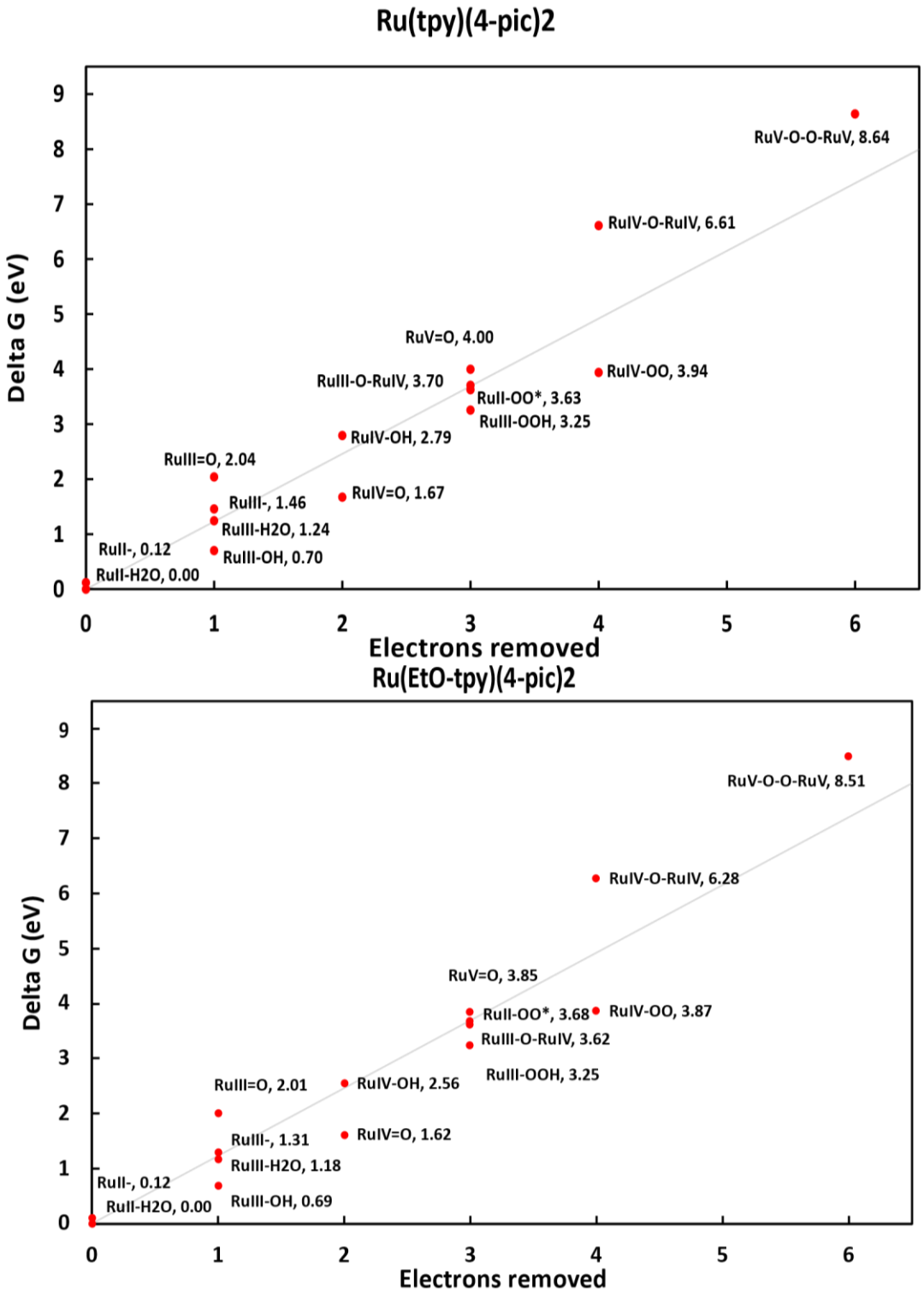

Figure 9. Latimer Frost diagrams of intermediates of **1** (A) and **2** (B), including possible O-O bond formation pathways. Line is a slope of +1.23 eV per electron.

This article is protected by copyright. All rights reserved

1864564x, 2022, 4, Downloaded from https://chemistry-europe.onlinelibrary.wiley.com/doi/10.1002/cssc.202101657 by Office Of Scientific And Technical Information, Wiley Online Library on [28/09/2023]. See the Terms and Conditions (https://onlinelibrary.wiley.com/terms-and-conditions) on Wiley Online Library for rules of use; OA articles are governed by the applicable Creative Commons License

Author Manuscript

Table 2. Changes in Free Energies of reaction of different intermediates, computed by DFT UB3LYP with CPCM water solution. Basis set for Ru is dgdzvp, and basis set for light atoms is 6-31G*.

Redox Potentials, V		
Species	**2**	**1**
$Ru^{II} \rightarrow Ru^{III} + e^-$	1.19	1.33
$Ru^{II}\text{-}H_2O \rightarrow Ru^{III}\text{-}H_2O + e^-$	1.30	1.38
$Ru^{II}\text{-}H_2O \rightarrow Ru^{III}\text{-}OH + e^- + H^+$	0.69	0.70
$Ru^{III}\text{-}H_2O \rightarrow Ru^{IV}\text{-}OH + e^- + H^+$	1.26	1.42
$Ru^{III}\text{-}OH \rightarrow Ru^{IV}=O + e^- + H^+$	0.94	0.97
$Ru^{III}\text{-}OH \rightarrow Ru^{IV}\text{-}OH + e^-$	1.87	2.09
$^{T}\, Ru^{IV}=O \rightarrow Ru^{V}=O + e^-$	2.23	2.33
$^{S}\, Ru^{IV}=O \rightarrow Ru^{V}=O + e^-$	1.47	1.57
$Ru^{IV}\text{-}OH \rightarrow Ru^{V}=O + e^- + H^+$	1.29	1.21
$Ru^{III}\text{-}OOH \rightarrow Ru^{IV}\text{-}OO + e^- + H^+$	0.62	0.68
Free energies of Reaction, eV		
$Ru^{II} + H_2O \rightarrow Ru^{II}\text{-}H_2O$	-0.12	-0.13
$Ru^{III} + H_2O \rightarrow Ru^{III}\text{-}H_2O$	-0.01	-0.08
$Ru^{IV}=O + H_2O \rightarrow Ru^{II}\text{-}OOH + H^+$	1.76	1.63
$Ru^{V}=O + H_2O \rightarrow Ru^{III}\text{-}OOH + H^+$	-0.60	-0.74
$Ru^{III}\text{-}OOH \rightarrow Ru^{II}\text{-}OO^{\bullet -} + H^+$	0.43	0.37
$Ru^{IV}=O\ ^{T} \rightarrow Ru^{IV}=O\ ^{S}$	0.76	0.76

Conclusion

Understanding the exact mechanisms of O-O bond formation in catalytic systems leads to systematic development of the more active catalysts. The addition of electron-donating moieties into the ligand backbone of water oxidation catalysts may increase oxygen evolution rates. We produced and analyzed experimental and computational data on the $[Ru(tpy)(pic)_2(H_2O)]^{2+}$ and $[Ru(EtO\text{-}tpy)(pic)_2(H_2O)]^{2+}$ derived through simple electronic modification of the tpy backbone of the first catalyst. The addition of a single electron-donating

This article is protected by copyright. All rights reserved

Author Manuscript

1864564x, 2022, 4, Downloaded from https://chemistry-europe.onlinelibrary.wiley.com/doi/10.1002/cssc.202101657 by Office Of Scientific And Technical Information, Wiley Online Library on [28/09/2023]. See the Terms and Conditions (https://onlinelibrary.wiley.com/terms-and-conditions) on Wiley Online Library for rules of use; OA articles are governed by the applicable Creative Commons License

group (EtO) to the ligand backbone increased the catalyst's activity by at least factor of two. We also studied the photocatalytic water oxidation and demonstrated excellent catalytic activity. These results cross verify the reported literature that the increased rate of O_2 evolution in the presence of the -EtO group is likely due to the decreased redox potentials of the complex, easing access to a Ru^V=O state.[56,57] Kinetic data indicate that the O-O bond formation step likely occurs through a water nucleophilic attack process. Spectroscopic and computational analysis suggests that prior to O-O bond formation, the catalysts may achieve high-valent Ru^V intermediate via PCET from the Ru^{IV}-OH state. Density functional theory calculations, resonance Raman analysis, and XAS results provide insight to the structure of reactive intermediates under catalytic conditions. The results presented here inform the successful rational design and modification of mononuclear, transition-metal-based water oxidation catalysts.

Materials and Methods:

General Information:

All chemicals and solvents were purchased from Sigma Aldrich, AK Scientific and TCI America and used as received. NMR spectra were recorded on a Bruker AV-III-HD-400 400MHz spectrometer, and chemical shifts were referenced to solvent residual peaks. UV-vis spectra were recorded on a Varian Cary 300- Bio spectrophotometer. Aqueous solutions were prepared using ultrapure (Type 1) water (resistivity 18.2 MΩ·cm at 25 ◦C) from a Q-POD unit of Milli-Q integral water purification system (Millipore, Billerica, MA, USA). Solvents and chemicals were purchased from Sigma-Aldrich (St. Louis, MO, USA) and were used without further purification.

EPR:

X-band EPR measurements were performed on an EMX X-band spectrometer equipped with an X-Band CW microwave bridge (Bruker, Billerica, MA, USA). Samples were oxidized with ammonium cerium nitrate (Ce^{IV}) and frozen in liquid nitrogen within 30s. During EPR measurements, sample temperature was maintained at 20 K using a closed-cycle cryostat (ColdEdge Technologies, Allentown, PA, USA). Spectrometer conditions were as follows: microwave frequency 9.47 GHz; field modulation amplitude 10 G at 100 kHz, microwave power 31.7 mW, unless otherwise mentioned. Measurements were performed on the same day in the same conditions, to allow accurate comparison of signal intensities.

This article is protected by copyright. All rights reserved

Author Manuscript

1864564x, 2022, 4, Downloaded from https://chemistry-europe.onlinelibrary.wiley.com/doi/10.1002/cssc.202101657 by Office Of Scientific And Technical Information, Wiley Online Library on [28/09/2023]. See the Terms and Conditions (https://onlinelibrary.wiley.com/terms-and-conditions) on Wiley Online Library for rules of use; OA articles are governed by the applicable Creative Commons License

Electrochemistry:

Cyclic voltammetry was accomplished using a potentiostat (CHI 627C; CH Instruments Inc., Austin, TX, USA) using standard single-compartment 3-electrode cell. Boron-doped diamond electrode (BDD) having diameter 3 mm, served as working, a piece of a platinum wire in an auxiliary chamber served as the counter electrode, and saturated Ag/AgCl electrode served as the reference electrode. Electrolytes were saturated with argon prior to the measurements. The half-wave potentials ($E_{1/2}$) of the reported complexes in this work were determined as the average of the anodic and cathodic peak potentials ($E_{1/2} = (E_{pa} + E_{pc})/2$) from the cyclic voltammetry. From the peak-to-peak separations ΔE_p ($\Delta E_p = E_{pa} - E_{pc}$) as well as the ratio of the anodic to cathodic peak currents (i_{pa}/i_{pc}) the reversibility of the redox couples were determined. All reported measurements were repeated several times to ensure the reproducibility of results.

Resonance Raman spectroscopy:

For resonance Raman measurements, λ_{ex}= 442 nm from a HeCd laser was used. A Shamrock 303i spectrometer and Andor iDus 420 camera were used to record the spectra. The laser beam diameter on the sample was focused to 1 mm. The laser beam power was measured to be ~ 20 mW. The sample was at cryogenic temperature in a cryostage cooled with liquid nitrogen. To prevent sample from laser damage, the sample was moved to fresh position every 50 seconds. A grating with 1800 l/mm dispersed the scattered Raman signal. The spectrometer slit was open for 70 µm and an approximate resolution of ~5 cm^{-1} was achieved. The data was collected by averaging 3000 scans and each scan exposure time was 1 second.

Preparation of 2 in $H_2{}^{18}O$ samples for Raman spectroscopy: To prepare the 1 mM solution of complex **2** in $H_2{}^{18}O$ 0.66 mg of [Ru(EtO-tpy)(pic)$_2$Cl]Cl was dissolved 1 mL of $H_2{}^{18}O$ water and then was stirred overnight, followed by the addition of 0.42 mg of $AgNO_3$ (2.5 equiv.). After being stirred overnight, the solution was filtered through a 0.2 µm syringe filter to remove the AgCl precipitate. For the experiment 50 µL of the $H_2{}^{18}O$ solution of **2** was mixed with 5 µL of 200 mM CAN dissolved in 1 M HNO_3. Sample was frozen on the sapphire within 30 sec after mixing for measurements at cryogenic temperatures. The final enrichment of $H_2{}^{18}O$ after addition of HNO_3 and CAN was above 90 percent.

Mass Spectroscopy:

This article is protected by copyright. All rights reserved

1864564x, 2022, 4, Downloaded from https://chemistry-europe.onlinelibrary.wiley.com/doi/10.1002/cssc.202101657 by Office Of Scientific And Technical Information, Wiley Online Library on [28/09/2023]. See the Terms and Conditions (https://onlinelibrary.wiley.com/terms-and-conditions) on Wiley Online Library for rules of use; OA articles are governed by the applicable Creative Commons License

Author Manuscript

High resolution ESI mass spectra were recorded on a Waters UPLC SQD2 mass spectrometer (ESI MS and APCI MS).

O_2 Evolution:

Oxygen evolution was measured with a Clark-type polarographic oxygen electrode with an Oxygraph System (Hansatech Instruments Ltd., King's Lynn, Norfolk, UK). Calibration was performed by measuring signal in O_2-saturated deionized water and then adding sodium dithionite (an oxygen-depleting agent). The drop in the signal was set equal to the solubility of oxygen in water at room temperature (262 µmol/L).

In Chemical catalysis the borosilicate vessel was filled with 500 µL solutions of the complex at pH = 1 (in 0.1 M nitric acid) and was constantly stirred. 20 mM. of Ce^{IV} dissolved in nitric acid at pH = 1 was added to the chamber and oxygen concentration was recorded as a function of time

In photochemical catalysis the borosilicate vessel was filled with 500 µL solution of the complex (25µM to 100µM) in 0.1 M phosphate buffer (pH = 7) and constantly stirred. 1 mM of $[Ru^{II}(bpy)_3]$ and 0.1 M $Na_2S_2O_8$ at pH = 7 dissolved in 0.1 M phosphate buffer were added to the chamber. 60 W visible light illuminated the samples, and the oxygen concentration was recorded as a function of time.

DFT Calculation:

Density functional theory calculations were performed at the UB3LYP level of theory, with the DGDZVP basis set for the ruthenium atoms, and the 6-31G* basis set was used for light (C, H, N, O) atoms. All molecules were modelled in water using the Conductor Polarized Continuum Model (CPCM) solvation model. All redox potentials were calculated using the DFT-calculated free energies of the products minus the reactants. From this value, 4.44 V was subtracted to account for the NHE voltage. The free energy of solvation for H^+ was taken to be −11.64 eV. Geometries of intermediates are optimized, then electronic/thermal energies and vibrational frequencies are calculated as single-point calculations upon the optimized states. Optimization of dimerized geometries required use of quadratic convergence criteria.

Synthesis

The R-tpy ligands and the precursor complex $Ru(R\text{-}tpy)Cl_3$ were prepared following the literature procedure.

This article is protected by copyright. All rights reserved

Author Manuscript

1864564x, 2022, 4, Downloaded from https://chemistry-europe.onlinelibrary.wiley.com/doi/10.1002/cssc.202101657 by Office Of Scientific And Technical Information, Wiley Online Library on [28/09/2023]. See the Terms and Conditions (https://onlinelibrary.wiley.com/terms-and-conditions) on Wiley Online Library for rules of use; OA articles are governed by the applicable Creative Commons License

Synthesis of [Ru(R-tpy)(pic)$_2$Cl]Cl

A mixture of the precursor catalyst [Ru(R-tpy)Cl$_3$] (100 mg), 4-picoline (10 mL) and triethylamine (0.6 mL) was refluxed at 100 °C for 13 h. After cooling, the reaction mixture was treated by 10 mL of hexane to precipitate out the product. To remove the excess 4-picoline, the dark purple-colored precipitate was collected and washed with hexane (20 mL). The resulting solid was collected and purified by Chromatography on silica gel and eluted with EtOH:H_2O (3:1), followed by recrystallization, resulting a purple-colored solid. The collected compounds were characterized as [Ru(R-tpy)(pic)$_2$Cl]Cl by ^{1}H NMR and ^{13}C NMR.

Synthesis of [Ru(tpy)(pic)$_2$Cl]Cl: Yield: 80 mg, 60% based on Ru. HRMS (ESI): Calc. for $C_{27}H_{25}N_5ClRu$ [Ru(tpy)(4-pic)$_2$Cl]$^{2+}$m/z 556.08 found 556.26. ^{1}H NMR (DMSO-d6): δ 9.16 (d, 2H, J = 6.30 Hz), 8.66 (dd, 4H, J = 11.2 Hz), 8.13 (dd, 3H, J = 7.86 Hz), 7.98 (t, 2H, J = 8.2 Hz), 7.86 (t, 3H, J = 2.22 Hz), 7.78 (dd, 4H, J = 6.52 Hz), 6.906 (d, 3H, J = 6.16 Hz), 2.00 (s, 6H, CH_3). The 400 MHz ^{13}C NMR (δ, DMSO-d6): 20.39, 123.91, 124.46, 125.87, 128.97, 131.99, 137.67, 148.96, 151.17, 152.54, 158.85, 160.81.

Synthesis of [Ru(EtO-tpy)(pic)$_2$Cl]Cl: Yield: 78 mg**,** 60% based on Ru. HRMS (ESI): Calc. for $C_{29}H_{29}N_5OClRu$ [Ru(EtO-tpy)(4-pic)$_2$Cl]$^{2+}$m/z 600.11 found 600.084. ^{1}H NMR (DMSO-d6): δ 9.16 (t, 2H, J = 2.68 Hz), 8.69 (d, 2H, J = 7.96Hz), 8.41 (s, 2H), 8.12 (d, 2H, J = 1.6 Hz), 7.77 (t, 6H, J = 6.6 Hz), 6.91 (d, 4H, J = 6 Hz), 4.42 (d, 2H, J = 6.96 Hz), 2.10 (s, 6H, CH_3), 1.46 (t, 3H, J = 11.2). The 400 MHz ^{13}C NMR (δ, DMSO-d6): 14.73, 20.38, 45.78, 111.48, 122.02, 124.67, 125.77, 128.90, 137.34, 148.58, 151.40, 152.90, 159.67, 160.86.

Preparation of 1 mM of [Ru(tpy)(pic)$_2$H$_2$O](NO$_3$)$_2$

To prepare the 1 mM solution of complex **1,** 6.6 mg of [Ru(tpy)(pic)$_2$Cl]Cl was dissolved 10 ml of de-ionized water and then was stirred overnight, followed by the addition of 4.2 mg of AgNO3 (2.5 equiv.). After being stirred overnight, the solution was filtered through a 0.2 µm syringe filter to remove the AgCl precipitate. Water was removed under vacuum, remaining compound was dissolved with DMSO-d6 and was characterized by ^{1}H NMR and ^{13}C NMR. Uv-vis: λmax = 508 nm. HRMS (ESI): Calc. for $C_{27}H_{27}N_5ORu$ [Ru(tpy)(4-pic)$_2$(H_2O)]$^{2+}$m/z 539.13 found 539.39. ^{1}H NMR (DMSO-d6): δ: 9.17 (d, 1H, J = 4.8 Hz), 8.78 (d, 2H, J = 6.4 Hz), 8.68 (t, 2H, J = 8 Hz), 8.36 (m, 1H), 8.16 (t, 2H, J = 7.68 Hz), 8.02 (t, 1H, J = 7.94 Hz), 7.9 (t, 1H), 7.84 (t, 1H) 7.57 (d, 2H, J = 5.24 Hz), 7.5 (d, 2H, J = 4.96 Hz), 7.08 (d, 2H, J = 4.88 Hz), 6.97 (d, 2H, J = 5.12 Hz), 2.14 (s, 6H). The 400 MHz ^{13}C NMR (δ, DMSO-d6):

This article is protected by copyright. All rights reserved

Author Manuscript

1864564x, 2022, 4, Downloaded from https://chemistry-europe.onlinelibrary.wiley.com/doi/10.1002/cssc.202101657 by Office Of Scientific And Technical Information, Wiley Online Library on [28/09/2023]. See the Terms and Conditions (https://onlinelibrary.wiley.com/terms-and-conditions) on Wiley Online Library for rules of use; OA articles are governed by the applicable Creative Commons License

20.53, 124.76, 126.37, 126.57, 126.79, 127.75, 130.12, 140.61, 150.46, 150.70, 151.18, 151.96, 155.76, 156.24.

Preparation of 1 mM of [Ru(EtO-tpy)(pic)$_2$H$_2$O](NO$_3$)$_2$

To prepare the 1 mM solution of complex **2,** 7 mg of [Ru(EtO-tpy)(pic)$_2$Cl]Cl was dissolved 10 ml of de-ionized water and then was stirred overnight, followed by the addition of 4.2 mg of AgNO3 (2.5 equiv.). After being stirred overnight, the solution was filtered through a 0.2 µm syringe filter to remove the AgCl precipitate. Water was removed under vacuum, remaining compound was dissolved with DMSO-d6 and was characterized by ^{1}H NMR and ^{13}C NMR. Uv-vis: λmax = 516 nm. HRMS (ESI): Calc. for $C_{27}H_{25}N_5ClRu$ [Ru(EtO-tpy)(4-pic)$_2$(H$_2$O)]$^{2+}$m/z 583.15 found 583.16. ^{1}H NMR (DMSO-d6): 9.34 (s, 1H), 9.19 (s, 1H), 8.83 (d, 1H, J = 6.12 Hz), 8.72 (d, 1H, J = 7.8 Hz), 8.42 (s, 2H), 8.32 (t, 2H, J = 3.4 Hz), 8.13 (t, 1H, J = 7.4 Hz), 7.87 (t, 1H), 7.80 (t, 1H) 7.59 (d, 2H, J = 76.4 Hz), 7.5 (d, 2H, J = 6.4 Hz), 7.08 (d, 2H, J = 4.76 Hz), 6.97 (d, 2H, J = 3.24 Hz), 4.42 (d, 2H, J = 5.68 Hz), 2.15 (d, 6H, J = 3.6 Hz), 1.43 (t, 3H, J = 6.8 Hz),. The 400 MHz ^{13}C NMR (δ, DMSO-d6): 8.99, 20.53, 46.13, 111.81, 127.60, 127.69, 129.98, 140.47, 151.04, 151.99, 156.35, 156.36, 157.97, 168.15.

Associated content

Supporting Information.

Author information

Corresponding author: ypushkar@purdue.edu

Acknowledgments

This research was supported by NSF, CHE-1900476 (Y.P.). The use of the Advanced Photon Source, an Office of Science User Facility operated by the U.S. Department of Energy (DOE) Office of Science by Argonne National Laboratory, was supported by the U.S. DOE under Contract DE-AC02- 06CH11357. The PNC/XSD (Sector 20) facilities at the Advanced Photon Source and research at these facilities were supported by the U.S. Department of Energy, Basic Energy Science and the Canadian Light Source. Access to EPR was provided by the Amy Instrumentation Facility, Department of Chemistry, under the supervision of Dr. Michael Everly. We acknowledge Oliver Carey for his assistance in recording resonance Raman spectra.

This article is protected by copyright. All rights reserved

Author Manuscript

1864564x, 2022, 4, Downloaded from https://chemistry-europe.onlinelibrary.wiley.com/doi/10.1002/cssc.202101657 by Office Of Scientific And Technical Information, Wiley Online Library on [28/09/2023]. See the Terms and Conditions (https://onlinelibrary.wiley.com/terms-and-conditions) on Wiley Online Library for rules of use; OA articles are governed by the applicable Creative Commons License

References:

[1] N. S. Lewis, D. G. Nocera *PNAS* **2006**, *103*, 15729-15735.
[2] T. R. Cook, D. K. Dogutan, S. Y. Reece, Y. Surendranath, T. S. Teets, D. G. Nocera *Chem. Rev.* **2010**, *110*, 6474-6502.
[3] M. Gratzel *Acc. Chem. Res.* **1981**, *14*, 376-384.
[4] A. J. Bard, M. A. Fox *Acc. Chem. Res.* **1995**, *28*, 141-145.
[5] M. Wang, L. Chen, L. Sun *Energy Environ. Sci.* **2012**, *5*, 6763-6778.
[6] S. Chaudhuri, S. Mukhopadhyay, R. Banerjee *J. Chem. Soc., Dalton Trans.***1995**, 621-624.
[7] B. Loll, J. Kern, W. Saenger, A. Zouni, J. Biesiadka *Nature*. **2005**, *438*, 1040-1044.
[8] J. J. Concepcion, R. L. House, J. M. Papanikolas, T. J. Meyer *PNAS* **2012**, *109*, 15560-15564.
[9] P. E. M. Siegbahn, R. H. Crabtree *J. Am. Chem. Soc.* **1999**, *121*, 117-127.
[10] J. Patel, K. Majee, E. Ahmad, K. Tanaka, S. K. Padhi *Dalton Trans.* **2015**, *44*, 920-923.
[11] J. Patel, K. Majee, S. K. Padhi *Rsc Adv*. **2016**, *6*, 61959-61965.
[12] J. Patel, K. Majee, E. Ahmad, B. Das, S. K. Padhi *Eur. J. Inorg. Chem.* **2017**, 160-171.
[13] J. Patel, K. Majee, M. Raj, A. Vatsa, S. Rai, S. K. Padhi *ChemistrySelect*. **2017**, *2*, 3053-3059.
[14] J. Patel, K. Majee, E. Ahmad, A. Vatsa, B. Das, S. K. Padhi *ChemistrySelect*. **2017**, *2*, 123-129.
[15] J. Chen, P. Wagner, L. Tong, G. G. Wallace, D. L. Officer, G. F. Swiegers *Angew. Chem. Int. Ed.***2012**, *51*, 1907-1910.
[16] R. Brimblecombe, G. F. Swiegers, G. C. Dismukes, L. Spiccia *Angew. Chem. Int. Ed.***2008**, *47*, 7335-7338.
[17] Y. Gao, J. Liu, M. Wang, Y. Na, B. Akermark, L. Sun *Tetrahedron*. **2007**, *63*, 1987-1994.
[18] L. Mognon, S. Mandal, C. E. Castillo, J. Fortage, F. Molton, G. Aromi, J. Benet-Buchhlolz, M.-N. Collombcd, A. Llobet *Chem. Sci.* **2016**, *7*, 3304-3312.
[19] K. J. Young, M. K. Takase, G. W. Brudvig *Inorg. Chem.***2013**, *52*, 7615-7622.
[20] A. Chanda, X. P. Shan, M. Chakrabarti, W. C. Ellis, D. L. Popescu, F. T. de Oliveira, D. Wang, L. Que, T. J. Collins, E. Munck, E. L. Bominaar *Inorg. Chem.***2008**, *47*, 3669-3678.
[21] R. Ezhov, A. K. Ravari, Y. Pushkar *Angew. Chem.-Int. Edit.* **2020**, *59*, 13502-13505.
[22] S. I. Shylin, M. V. Pavliuk, L. D'Amario, F. Mamedov, J. Sa, G. Berggren, I. O. Fritsky *Commun. Chem.* **2019**, *55*, 3335-3338.
[23] C. Panda, J. Debgupta, D. D. Diaz, K. K. Singh, S. S. Gupta, B. B. Dhar *J. Am. Chem. Soc.* **2014**, *136*, 12273-12282.
[24] A. Bucci, A. Savini, L. Rocchigiani, C. Zuccaccia, S. Rizzato, A. Albinati, A. Llobet, A. Macchioni *Organometallics*. **2012**, *31*, 8071-8074.
[25] D. B. Grotjahn, D. B. Brown, J. K. Martin, D. C. Marelius, M. C. Abadjian, H. N. Tran, G. Kalyuzhny, K. S. Vecchio, Z. G. Specht, S. A. Cortes-Llamas, V. Miranda-Soto, C. van Niekerk, C. E. Moore, A. L. Rheingold *J. Am. Chem. Soc.* **2011**, *133*, 19024-19027.
[26] H. Junge, N. Marquet, A. Kammer, S. Denurra, M. Bauer, S. Wohlrab, F. Gaertner, M.-M. Pohl, A. Spannenberg, S. Gladiali, M. Beller *Chem. Eur. J.* **2012**, *18*, 12749-12758.
[27] A. Petronilho, M. Rahman, J. A. Woods, H. Al-Sayyed, H. Mueller-Bunz, J. M. D. MacElroy, S. Bernhard, M. Albrecht *Dalton Trans.* **2012**, *41*, 13074-13080.
[28] D. L. Ashford, M. K. Gish, A. K. Vannucci, M. K. Brennaman, J. L. Templeton, J. M. Papanikolas, T. J. Meyer *Chem. Rev.* **2015**, *115*, 13006-13049.
[29] J. J. Concepcion, J. W. Jurss, P. G. Hoertz, T. J. Meyer *Angew. Chem. Int. Ed.***2009**, *48*, 9473-9476.
[30] M. R. Norris, J. J. Concepcion, D. P. Harrison, R. A. Binstead, D. L. Ashford, Z. Fang, J. L. Templeton, T. J. Meyer *J. Am. Chem. Soc.* **2013**, *135*, 2080-2083.
[31] W. J. Youngblood, S.-H. A. Lee, Y. Kobayashi, E. A. Hernandez-Pagan, P. G. Hoertz, T. A. Moore, A. L. Moore, D. Gust, T. E. Mallouk *J. Am. Chem. Soc.* **2009**, *131*, 926-927.
[32] H. Luo, Z. Zeng, G. Zeng, C. Zhang, R. Xiao, D. Huang, C. Lai, M. Cheng, W. Wang, W. Xiong, Y. Yang, L. Qin, C. Zhou, H. Wang, Y. Zhou, S. Tian *Chem. Eng. J.* **2020**, *383*.
[33] S. Mukhopadhyay, O. Basu, R. Nasani, S. K. Das *Commun. Chem.* **2020**, *56*, 11735-11748.

This article is protected by copyright. All rights reserved

Author Manuscript

1864564x, 2022, 4, Downloaded from https://chemistry-europe.onlinelibrary.wiley.com/doi/10.1002/cssc.202101657 by Office Of Scientific And Technical Information, Wiley Online Library on [28/09/2023]. See the Terms and Conditions (https://onlinelibrary.wiley.com/terms-and-conditions) on Wiley Online Library for rules of use; OA articles are governed by the applicable Creative Commons License

[34] S. Lin, Y. Pineda-Galvan, W. A. Maza, C. C. Epley, J. Zhu, M. C. Kessinger, Y. Pushkar, A. J. Morris *ChemSusChem*. **2017**, *10*, 514-522.
[35] Z. N. Zahran, Y. Tsubonouchi, E. A. Mohamed, M. Yagi *Chemsuschem*. **2019**, *12*, 1775-1793.
[36] Y. Horiuchi, T. Toyao, K. Miyahara, L. Zakary, V. Dang Do, Y. Kamata, T.-H. Kim, S. W. Lee, M. Matsuoka *Commun. Chem.* **2016**, *52*, 5190-5193.
[37] D. Lebedev, Y. Pineda-Galvan, Y. Tokimaru, A. Fedorov, N. Kaeffer, C. Coperet, Y. Pushkar *J. Am. Chem. Soc.* **2018**, *140*, 451-458.
[38] R. Ezhov, A. K. Ravari, A. Page, Y. Pushkar *ACS Catal.* **2020**, *10*, 5299-5308.
[39] Q. Zeng, F. W. Lewis, L. M. Harwood, F. Hartl *Coord. Chem. Rev.* **2015**, *304*, 88-101.
[40] R. Cao, W. Lai, P. Du *Energy Environ. Sci.* **2012**, *5*, 8134-8157.
[41] M. D. Karkas, O. Verho, E. V. Johnston, B. Akermark *Chem. Rev.* **2014**, *114*, 11863-12001.
[42] J. M. Kamdar, D. B. Grotjahn *Molecules*. **2019**, *24*.
[43] R. Matheu, M. Z. Ertem, C. Gimbert-Surinach, X. Sala, A. Llobet *Chem. Rev.* **2019**, *119*, 3453-3471.
[44] D. Moonshiram, I. Alperovich, J. J. Concepcion, T. J. Meyer, Y. Pushkar *PNAS* **2013**, *110*, 3765-3770.
[45] S. W. Gersten, G. J. Samuels, T. J. Meyer *J. Am. Chem. Soc.* **1982**, *104*, 4029-4030.
[46] J. A. Gilbert, D. S. Eggleston, W. R. Murphy, D. A. Geselowitz, S. W. Gersten, D. J. Hodgson, T. J. Meyer *J. Am. Chem. Soc.* **1985**, *107*, 3855-3864.
[47] D. Moonshiram, V. Purohit, J. J. Concepcion, T. J. Meyer, Y. Pushkar *Materials*. **2013**, *6*, 392-409.
[48] N. Kaveevivitchai, R. Zong, H.-W. Tseng, R. Chitta, R. P. Thummel *Inorg. Chem.***2012**, *51*, 2930-2939.
[49] S. Bensaid, G. Centi, E. Garrone, S. Perathoner, G. Saracco *ChemSusChem*. **2012**, *5*, 500-521.
[50] N. Kaveevivitchai, R. Chitta, R. F. Zong, M. El Ojaimi, R. P. Thummel *J. Am. Chem. Soc.* **2012**, *134*, 10721-10724.
[51] Y. H. Xu, L. L. Duan, L. P. Tong, B. Akermark, L. C. Sun *Commun. Chem.* **2010**, *46*, 6506-6508.
[52] L. Wang, L. L. Duan, L. P. Tong, L. C. Sun *J. Catal.* **2013**, *306*, 129-132.
[53] D. J. Wasylenko, C. Ganesamoorthy, M. A. Henderson, B. D. Koivisto, H. D. Osthoff, C. P. Berlinguette *J. Am. Chem. Soc.* **2010**, *132*, 16094-16106.
[54] D. J. Wasylenko, C. Ganesamoorthy, B. D. Koivisto, M. A. Henderson, C. P. Berlinguette *Inorg. Chem.***2010**, *49*, 2202-2209.
[55] D. J. Wasylenko, R. D. Palmer, C. P. Berlinguette *Commun. Chem.* **2013**, *49*, 218-227.
[56] M. Yagi, S. Tajima, M. Komi, H. Yamazaki *Dalton Trans.* **2011**, *40*, 3802-3804.
[57] A. K. Ravari, G. B. Zhu, R. Ezhov, Y. Pineda-Galvan, A. Page, W. Weinschenk, L. F. Yan, Y. Pushkar *J. Am. Chem. Soc.* **2020**, *142*, 884-893.
[58] Y. Pushkar, D. Moonshiram, V. Purohit, L. F. Yan, I. Alperovich *J. Am. Chem. Soc.* **2014**, *136*, 11938-11945.
[59] L. Duan, A. Fischer, Y. Xu, L. Sun *J. Am. Chem. Soc.* **2009**, *131*, 10397-+.
[60] L. Wang, L. Duan, B. Stewart, M. Pu, J. Liu, T. Privalov, L. Sun *Abstr. Pap. Am. Chem. Soc.* **2013**, *245*.
[61] L. Wang, L. Duan, L. Tong, L. Sun *J. Catal.* **2013**, *306*, 129-132.
[62] L. L. Duan, F. Bozoglian, S. Mandal, B. Stewart, T. Privalov, A. Llobet, L. C. Sun *Nature Chemistry*. **2012**, *4*, 418-423.
[63] L. L. Duan, C. M. Araujo, M. S. G. Ahlquist, L. C. Sun *PNAS* **2012**, *109*, 15584-15588.
[64] L. Wang, L. Duan, Y. Wang, M. S. G. Ahlquist, L. C. Sun *Commun. Chem.* **2014**, *50*, 12947-12950.
[65] L. L. Duan, Y. H. Xu, P. Zhang, M. Wang, L. C. Sun *Inorg. Chem.***2010**, *49*, 209-215.
[66] B. Zhang, L. Sun *J. Am. Chem. Soc.* **2019**, *141*, 5565-5580.
[67] Y. Xie, D. Shaffer, A. Lewandowska-Andralojc, D. Szalda, J. Concepcion *Abstr. Pap. Am. Chem. Soc.* **2016**, *252*.
[68] R. Matheu, M. Z. Ertem, J. Benet-Buchholz, E. Coronado, V. S. Batista, X. Sala, A. Llobet *J. Am. Chem. Soc.* **2015**, *137*, 10786-10795.

This article is protected by copyright. All rights reserved

Author Manuscript

1864564x, 2022, 4, Downloaded from https://chemistry-europe.onlinelibrary.wiley.com/doi/10.1002/cssc.202101657 by Office Of Scientific And Technical Information, Wiley Online Library on [28/09/2023]. See the Terms and Conditions (https://onlinelibrary.wiley.com/terms-and-conditions) on Wiley Online Library for rules of use; OA articles are governed by the applicable Creative Commons License

[69] K. J. Takeuchi, M. S. Thompson, D. W. Pipes, T. J. Meyer *Inorg. Chem.***1984**, *23*, 1845-1851.
[70] H. W. Tseng, R. Zong, J. T. Muckerman, R. Thummel *Inorg. Chem.***2008**, *47*, 11763-11773.
[71] L. P. Tong, R. F. Zong, R. W. Zhou, N. Kaveevivitchai, G. Zhang, R. P. Thummel *Faraday Discuss.* **2015**, *185*, 87-104.
[72] Y. Y. Liu, S. M. Ng, S. M. Yiu, W. W. Y. Lam, X. G. Wei, K. C. Lau, T. C. Lau *Angew. Chem.-Int. Edit.* **2014**, *53*, 14468-14471.
[73] Y. Pineda-Galvan, A. K. Ravari, S. Shmakov, L. Lifshits, N. Kaveevivitchai, R. Thummel, Y. Pushkar *J. Catal.* **2019**, *375*, 1-7.
[74] D. Moonshiram, Y. Pineda-Galvan, D. Erdman, M. Palenik, R. Zong, R. Thummel, Y. Pushkar *J. Am. Chem. Soc.* **2016**, *138*, 15605-15616.
[75] D. Moonshiram, J. W. Jurss, J. J. Concepcion, T. Zakharova, I. Alperovich, T. J. Meyer, Y. Pushkar *J. Am. Chem. Soc.* **2012**, *134*, 4625-4636.
[76] A. K. Ravari, G. Zhu, R. Ezhov, Y. Pineda-Galvan, A. Page, W. Weinschenk, L. Yan, Y. Pushkar *J. Am. Chem. Soc.* **2020**, *142*, 884-893.
[77] Y. Pushkar, Y. Pineda-Galvan, A. K. Ravari, T. Otroshchenko, D. A. Hartzler *J. Am. Chem. Soc.* **2018**, *140*, 13538-13541.
[78] Y. Pineda-Galvan, A. K. Ravari, S. Shmakov, L. Lifshits, N. Kaveevivitchai, R. Thummel, Y. Pushkar *J. Catal.* **2019**, *375*, 1-7.
[79] B. P. Sullivan, J. M. Calvert, T. J. Meyer *Inorg. Chem.***1980**, *19*, 1404-1407.

Author Manuscript

1864564x, 2022, 4, Downloaded from https://chemistry-europe.onlinelibrary.wiley.com/doi/10.1002/cssc.202101657 by Office Of Scientific And Technical Information, Wiley Online Library on [28/09/2023]. See the Terms and Conditions (https://onlinelibrary.wiley.com/terms-and-conditions) on Wiley Online Library for rules of use; OA articles are governed by the applicable Creative Commons License

This article is protected by copyright. All rights reserved